HHS Public Access
Author manuscript
Sci Immunol. Author manuscript; available in PMC 2024 November 17.

Published in final edited form as:
Sci Immunol. 2024 May 17; 9(95): eadi5374. doi:10.1126/sciimmunol.adi5374.

TREM2 deficiency reprograms intestinal macrophages and microbiota to enhance anti–PD-1 tumor immunotherapy

Blanda Di Luccia[1,2,†], **Martina Molgora**[1,*,†], **Darya Khantakova**[1,†], **Natalia Jaeger**[1,‡], **Hao-Wei Chang**[1,3], **Rafael S. Czepielewski**[1,‡], **Beth A. Helmink**[4,§], **Emily J. Onufer**[4], **José L. Fachi**[1], **Bishan Bhattarai**[1], **Tihana Trsan**[1], **Patrick F. Rodrigues**[1], **JinChao Hou**[1], **Jennifer K. Bando**[1,2], **Cristiane Sécca da Silva**[1], **Marina Cella**[1], **Susan Gilfillan**[1], **Robert D. Schreiber**[1], **Jeffrey I. Gordon**[1,3,5], **Marco Colonna**[1,*]

[1]Department of Pathology and Immunology, Washington University School of Medicine in Saint Louis, St. Louis, MO 63110, USA.

[2]Department of Microbiology and Immunology, Stanford University, Stanford, CA 94305, USA.

[3]Edison Family Center for Genome Sciences and Systems Biology, Washington University School of Medicine, St. Louis, MO 63110, USA.

[4]Department of Surgery, Washington University School of Medicine, St. Louis, MO 63110, USA.

[5]Center for Gut Microbiome and Nutrition Research, Washington University School of Medicine, St. Louis, MO 63110, USA.

Abstract

The gut microbiota and tumor-associated macrophages (TAMs) affect tumor responses to anti–programmed cell death protein 1 (PD-1) immune checkpoint blockade. Reprogramming TAM by either blocking or deleting the macrophage receptor triggering receptor on myeloid cells 2 (TREM2) attenuates tumor growth, and lack of functional TREM2 enhances tumor elimination by anti–PD-1. Here, we found that anti–PD-1 treatment combined with TREM2 deficiency in mice induces proinflammatory programs in intestinal macrophages and a concomitant

*Corresponding author. martina.molgora@wustl.edu (M.M.); mcolonna@wustl.edu (M.C.).
†These authors contributed equally to this work.
‡Present address: Immunology Center of Georgia, Medical College of Georgia, Department of Physiology, Augusta University, Augusta, GA 30912 USA.
§Present address: Department of Surgical Oncology, University of Texas MD Anderson Cancer Center, Houston, TX 77030 USA.

Author contributions: B.D.L., M.M., and D.K. performed experiments and analyzed the data. H.-W.C., R.S.C., B.A.H., E.J.O., J.L.F., B.B., T.T., P.F.R., J.H., J.B., and C.S.d.S. performed experiments. N.J. and H.-W.C. performed in silico analysis. S.G. bred, maintained, and validated the *Trem2*$^{-/-}$ mouse colony. S.G., M. Cella, R.D.S., and J.I.G. provided expertise. B.D.L., M.M., D.K., and M. Colonna conceptualized and wrote the paper with input from all coauthors.

Competing interests: M. Colonna is a member of the Vigil Neuro scientific advisory board, is a consultant for Cell Signaling Technology, received research grants from Vigil Neuro during the conduct of the study, and has a patent to TREM2 pending (PCT/US2021/019914). All other authors declare that they have no competing interests.

Supplementary Materials
This PDF file includes:
Figs. S1 to S10
Table S1
Other Supplementary Material for this manuscript includes the following:
Data files S1 to S7
MDAR Reproducibility Checklist

expansion of *Ruminococcus gnavus* in the gut microbiota. Gavage of wild-type mice with *R. gnavus* enhanced anti–PD-1–mediated tumor elimination, recapitulating the effect occurring in the absence of TREM2. A proinflammatory intestinal environment coincided with expansion, increased circulation, and migration of TNF-producing $CD4^+$ T cells to the tumor bed. Thus, TREM2 remotely controls anti–PD-1 immune checkpoint blockade through modulation of the intestinal immune environment and microbiota, with *R. gnavus* emerging as a potential probiotic agent for increasing responsiveness to anti-PD-1.

INTRODUCTION

Immune checkpoint inhibitors (CPIs) that block programmed cell death protein 1 (PD-1), programmed death-ligand 1 (PD-L1), and cytotoxic T lymphocyte–associated protein–4 (CTLA-4) are successfully used to activate antitumor T cell responses in the treatment of several types of cancers (1–3). However, although many patients respond durably to CPIs, a substantial number remain unresponsive or undergo recurrence, prompting the investigation of complementary therapeutic avenues to improve CPIs (3). Tumor-associated macrophages (TAMs) can support tumor cell survival and proliferation and angiogenesis and suppress the immune response, which ultimately hampers CPI efficacy (4, 5). Strategies targeting TAMs increase sensitivity to CPIs in mouse models and are currently being tested in clinical trials (4). Genetic deletion or antibody-mediated blockade of triggering receptor on myeloid cells 2 (TREM2), a receptor broadly expressed on TAMs, attenuates TAM immunosuppressive function (6–9) and augments antitumor T cell responses induced by anti–PD-1 (6).

Another strategy to improve CPI therapy relies on targeting the intestinal microbiota (10–13). Many studies have reported that the composition of the microbiota correlates with CPI efficacy in preclinical models and patients with cancer (10–12). Fecal microbiota transplant (FMT) or oral gavage with specific bacteria can increase sensitivity to CPIs in mouse models. Human studies found associations between the gut microbiota and effectiveness of CPIs in patients with cancer (10–12, 14) and more recently provided evidence of a causal relationship (15, 16). Specific members of the gut microbiota have been identified as probiotic strains that can boost antitumor T cell responses and alleviate TAM immunosuppression during CPI therapy (11, 12, 14).

Here, we found that the enhanced responsiveness of tumors to anti–PD-1 in TREM2-deficient mice is dependent on the microbiota. Administration of anti–PD-1 in *Trem2*$^{-/-}$ mice bearing subcutaneous tumors induced an expansion of *Ruminococcus gnavus* that was associated with remodeling of intestinal macrophages toward a proinflammatory phenotype and accumulation of tumor necrosis factor (TNF)–producing $CD4^+$ T cells. These changes in the intestinal microenvironment corresponded with the migration of TNF-producing $CD4^+$ T cells from the gut and systemic circulation into tumor-draining lymph nodes (dLNs), as well as improved control of tumor growth. We conclude that anti–PD-1 together with TREM2 deficiency causes a distinct response in the intestinal microenvironment that affects CPI therapy with a beneficial effect on tumor rejection.

RESULTS

TREM2's impact on tumor response to anti–PD-1 is influenced by the intestinal microbiota

We sought to determine whether the intestinal microbiota affects the beneficial effect of TREM2 deficiency in tempering tumor growth. Eight-week-old conventionally raised *Trem2*$^{+/+}$ and *Trem2*$^{-/-}$ mice co-housed from birth were inoculated subcutaneously with the methylcholanthrene (MCA)/1956 sarcoma cell line and immediately divided into two groups: In one group, *Trem2*$^{+/+}$ and *Trem2*$^{-/-}$ mice were kept co-housed (Coh) throughout the experiment (*Trem2*$^{+/+}$-Coh and *Trem2*$^{-/-}$-Coh); in another group, *Trem2*$^{+/+}$ and *Trem2*$^{-/-}$ mice were separated (Sep) after tumor injection (day 0) (*Trem2*$^{+/+}$-Sep and *Trem2*$^{-/-}$-Sep) (Fig. 1A). Litters from different genotypes derived from co-housed pregnant mothers were cross-fostered to avoid a potential effect of the maternal microbiota. All animals consumed a standard polysaccharide-rich mouse chow ad libitum. In both groups, *Trem2*$^{-/-}$ mice had a mild reduction of tumor burden compared with *Trem2*$^{+/+}$ mice, which was similar to that previously reported (fig. S1, A and B; $n = 5$ or 6 animals per group) (6). Because TREM2 deficiency also enhances the efficacy of anti–PD-1 treatment (6) and given the contribution of the gut microbiota to CPI therapy (6, 13), we examined the impact of housing conditions in these settings. *Trem2*$^{+/+}$ and *Trem2*$^{-/-}$ mice were inoculated with MCA/1956, divided into Coh and Sep groups, and then treated with anti–PD-1, starting at day 9 (Fig. 1A). *Trem2*$^{-/-}$-Sep had an enhanced response to anti–PD-1 compared with *Trem2*$^{+/+}$-Sep (Fig. 1B and fig. S1C). However, *Trem2*$^{-/-}$-Coh and *Trem2*$^{+/+}$-Coh mice responded similarly to anti–PD-1 (Fig.1B and fig. S1C).

The results from manipulating housing conditions raised the possibility that the effect of TREM2 deficiency in enhancing anti–PD-1–mediated tumor control could be related to the gut microbiota. Because *Trem2*$^{-/-}$-Sep and *Trem2*$^{+/+}$-Sep mice were separated just at the time of tumor inoculation, we determined whether the enhancing effect of TREM2 deficiency on anti–PD-1 could be further amplified by having *Trem2*$^{-/-}$ and *Trem2*$^{+/+}$ mice bred and hence born separately (*Trem2*$^{-/-}$–Sep-b; *Trem2*$^{+/+}$–Sep-b) rather than segregating them at the time of tumor inoculation. However, an equivalent increase in anti–PD-1 efficacy was evident in *Trem2*$^{-/-}$ mice that were separated from *Trem2*$^{+/+}$ mice either from birth or at the time of tumor inoculation (Fig. 1, C and D, and fig. S1D). Additionally, separation of *Trem2*$^{-/-}$ and *Trem2*$^{+/+}$ mice from birth did not amplify the difference in tumor growth between *Trem2*$^{-/-}$ and *Trem2*$^{+/+}$ mice in the absence of anti–PD-1 treatment (fig. S1E; $n = 4$ or 5 animals per group).

Because deletion or blockade of TREM2 together with anti–PD-1 enhances the accumulation of T cells in the MCA/1956 tumor model (6), we sought to determine whether T cell responses elicited by anti–PD-1 in *Trem2*$^{-/-}$ and *Trem2*$^{+/+}$ mice were also affected by housing conditions. *Trem2*$^{-/-}$-Sep mice injected with anti–PD-1 displayed an increase in intratumoral T cell frequency at two time points in comparison with *Trem2*$^{+/+}$-Sep mice, whereas no differences were noted between *Trem2*$^{-/-}$-Coh and *Trem2*$^{+/+}$-Coh mice (Fig. 1E and fig. S1F). The proportion of intratumoral CD4^{+}/CD8^{+} cells was similar in all conditions tested (fig. S1F). Additionally, T cell frequency and CD4^{+}/CD8^{+} proportion did not change significantly in tumor dLNs (fig. S1F). Together, these data raised the possibility that anti–

PD-1 induces changes in the microbiota of *Trem2*$^{-/-}$ mice that promote T cell enrichment within the tumor and augment anti–PD-1 efficacy.

To corroborate that anti–PD-1 induces de novo changes in the microbiota of *Trem2*$^{-/-}$ mice that enhance anti–PD-1 response, we performed microbiota transplantation experiments. Cecal contents of *Trem2*$^{-/-}$-Sep and *Trem2*$^{+/+}$-Sep mice were collected at the time of tumor inoculation [microbiota-d0 (mbt-d0)] and during tumor growth 3 days after initiation of PD-1 treatment [microbiota-d12 (mbt-d12)]. Cecal contents were introduced by oral gavage into either *Trem2*$^{+/+}$ or *Trem2*$^{-/-}$ mice that had been pretreated for 3 weeks with the VNAM (vancomycin, neomycin, ampicillin, and metronidazole) antibiotic cocktail. Seven days after the cecal microbial transplant (CMT), animals were subsequently inoculated with MCA/1956 and treated with anti–PD-1 (Fig. 2A). *Trem2*$^{+/+}$ recipients of mbt-d12 from *Trem2*$^{-/-}$ mice controlled tumor growth better than *Trem2*$^{+/+}$ mice that received mbt-d0 from *Trem2*$^{+/+}$ or *Trem2*$^{-/-}$ mice (Fig. 2B). Conversely, reconstitution of *Trem2*$^{-/-}$ mice with mbt-d0 or mbt-d12 from *Trem2*$^{+/+}$ mice delayed or completely abrogated their capacity to control tumor growth in comparison with *Trem2*$^{-/-}$ mice reconstituted with mbt-d0 from *Trem2*$^{-/-}$ mice. Overall, these results indicate that anti–PD-1 treatment in TREM2-deficient mice induces changes in intestinal microbiota that support tumor rejection.

Enrichment of *R. gnavus* is associated with TREM2 deficiency and improved tumor response to anti–PD-1

To identify key features in microbiota induced by anti–PD-1 in the TREM2-deficient background, we treated *Trem2*$^{-/-}$-Sep and *Trem2*$^{+/+}$-Sep with various antibiotics alone or in combination before tumor inoculation, separation, and anti–PD-1 treatment (Fig. 2C). Individually, ampicillin and vancomycin impaired the ability of *Trem2*$^{-/-}$-Sep mice to control tumor growth in response to anti–PD-1. Conversely, vehicle, metronidazole, or neomycin did not affect tumor control by *Trem2*$^{-/-}$-Sep mice (Fig. 2D and fig. S2). A mix of all four antibiotics (VNAM) completely abrogated the response to anti–PD-1 in both *Trem2*$^{-/-}$-Sep and *Trem2*$^{+/+}$-Sep mice (fig. S2); in fact, tumor growth was more robust than in any other condition, in agreement with the described requirement of the microbiota for CPIs to succeed (13, 17).

To further characterize the changes induced by TREM2 deficiency and anti–PD-1, we characterized mbt-d0 and mbt-d12 from *Trem2*$^{+/+}$-Sep, *Trem2*$^{-/-}$-Sep, *Trem2*$^{+/+}$-Coh, and *Trem2*$^{-/-}$-Coh tumor-bearing mice by variable region 4 (V4)–16*S* rRNA sequencing (data file S1). Principal coordinate analysis (PCoA) showed segregation of mbt-d12 collected from *Trem2*$^{-/-}$-Sep animals compared with those collected from *Trem2*$^{+/+}$-Sep, *Trem2*$^{-/-}$-Coh, and *Trem2*$^{+/+}$-Coh mice (Fig. 3A). PCoA plots of mbt-d12 and mbt-d0 communities from *Trem2*$^{-/-}$-Coh and *Trem2*$^{+/+}$-Coh mice showed differences that were significantly influenced by the treatment with anti–PD-1 (permutational multivariate analysis of variance, PERMANOVA: $P = 0.001$) but not by the genotype (PERMANOVA: $P = 0.238$) (fig. S3A). In contrast, differences between mbt-d12 and mbt-d0 among *Trem2*$^{-/-}$-Sep and *Trem2*$^{+/+}$-Sep or *Trem2*$^{-/-}$–Sep-b and *Trem2*$^{+/+}$–Sep-b were influenced by both the lack of TREM2 (PERMANOVA: $P = 0.001$) and the anti–PD-1 treatment (PERMANOVA: $P = 0.001$) (fig. S3, B and C). These findings demonstrate that *Trem2*$^{-/-}$ mice treated with anti–PD-1

develop a change in their gut microbiota that disappears when *Trem2*$^{-/-}$ and *Trem2*$^{+/+}$ mice are co-housed together.

To identify genotype and treatment discriminatory taxa, we performed an indicator species analysis of mbt-d12 collected from *Trem2*$^{+/+}$-Sep, *Trem2*$^{-/-}$-Sep, *Trem2*$^{-/-}$-Coh, and *Trem2*$^{+/+}$-Coh mice. An initial comparison between *Trem2*$^{+/+}$-Sep and *Trem2*$^{-/-}$-Sep microbiota highlighted 39 amplicon sequence variants (ASVs) that were significantly associated with *Trem2*$^{+/+}$-Sep and 23 ASVs that were significantly associated with *Trem2*$^{-/-}$-Sep mice (Fig. 3B; see data file S2 for statistical test results). Fewer ASVs were significantly associated with either *Trem2*$^{+/+}$-Coh or *Trem2*$^{-/-}$-Coh fecal microbiota (1 and 5, respectively; data file S3). To narrow down the number of ASVs in the *Trem2*$^{-/-}$-Sep microbiota that may enhance the anti–PD-1 response, we next compared ASVs in *Trem2*$^{-/-}$-Sep mice with those in *Trem2*$^{-/-}$-Coh animals where the enhanced response to anti–PD-1 was abolished. Eighteen ASVs were identified as selectively associated with *Trem2*$^{-/-}$-Sep; 10 of these were also significantly enriched in *Trem2*$^{-/-}$-Sep compared with *Trem2*$^{+/+}$-Sep mice (Fig. 3, B and C, and data file S4A) and represent taxa that belong to two distinct phyla (see data file S4B for taxonomy).

We further identified indicator species in mbt-d12 collected from *Trem2*$^{-/-}$-Sep mice treated with metronidazole, which does not diminish the enhanced response to anti–PD-1 (i.e., responses are comparable in metronidazole-treated and untreated *Trem2*$^{-/-}$-Sep mice; Fig. 3D and fig. S2A). Of the 10 ASVs enriched in *Trem2*$^{-/-}$-Sep versus *Trem2*$^{+/+}$-Sep and *Trem2*$^{-/-}$-Coh, only 1 ASV was significantly enriched in *Trem2*$^{-/-}$-Sep mice treated with metronidazole; this ASV was assigned to the anaerobic Gram-positive bacterium *R. gnavus* (Fig. 3D and data file S5). It should be noted that although *Trem2*$^{+/+}$-Sep microbiota contained *R. gnavus*, its mean percent relative abundance in *Trem2*$^{-/-}$-Sep mice was significantly higher (ASV.144: 0.68 ± 0.43%; ASV.102: 0.56 ± 0.27%) than the mean percentage detected in their *Trem2*$^{+/+}$-Sep counterparts (ASV.184: 0.27 ± 0.1%) after anti–PD-1 (fig. S3D). Moreover, when we compared the relative abundance of ASV.102 and ASV.144 associated with *Trem2*$^{-/-}$ mice between mbt-d0 and mbt-d12 (fig. S4, A to D), both ASVs were significantly increased after anti–PD-1 treatment (mbt-d12), supporting the idea that the presence of *R. gnavus* is not sufficient per se to promote the control of tumor growth. Instead, the relative abundance of *R. gnavus* in the microbial community must be considered. Together, these results demonstrate that anti–PD-1 treatment in TREM2-deficient mice biases microbiota composition toward an enrichment of specific species, with *R. gnavus* being closely associated with better control of tumor growth.

Given the growing interest in TREM2 blockade in oncological patients, we then asked whether anti-TREM2 treatment with a monoclonal antibody (mAb) in combination with anti–PD-1 in *wild-type* mice drove a similar effect to TREM2 deficiency in terms of modulation of the microbial communities. Anti-TREM2 treatment was associated with changes in the microbiota communities at several time points (days 0, 9, 12, and 18 after tumor injection) compared with mice treated with a control mAb (data file S6). However, we did not observe *R. gnavus* enrichment in any of the analyzed time points, suggesting that the contribution of the microbiome to the combined effect of anti-TREM2 and anti–PD-1 acute

blockade is not dependent on *R. gnavus* but might potentially rely on different species that act similarly to *R. gnavus*.

TREM2 deficiency in combination with anti–PD-1 blockade shifts the gut environment toward a proinflammatory state

Because an intestinal bloom of *R. gnavus* has been observed during active phases of inflammatory bowel disease (18), we investigated whether anti–PD-1 treatment in *Trem2*$^{-/-}$ mice may be associated with colon inflammation. Initially, we assessed weight loss and fecal lipocalin levels and found no significant differences between *Trem2*$^{+/+}$ and *Trem2*$^{-/-}$ mice whether or not they were treated with anti–PD-1 (fig. S5A). This suggested no clinical evidence of overt colitis in our model. To investigate potential subclinical inflammation, we conducted bulk RNA sequencing of colonic tissue and real-time polymerase chain reaction (PCR) analysis of selected cytokines. Principal components analysis (PCA) plots of sequenced samples showed that TREM2-deficient samples treated with anti–PD-1 clustered separately from the wild-type counterpart (fig. S5B), exhibiting an enrichment in pathways associated with cell activation, immune cell adhesion, T cell activation, and antigen presentation (fig. S5, C and D). Cytokine transcripts were below the detection limit, with the exception of *Tnf*, which was increased in the *Trem2*$^{-/-}$ group treated with anti–PD-1 (fig. S5E). Analysis of cytokine expression by real-time PCR showed a trend toward increased TNF, an increase in *Il17a*, and a decrease in *Il10* (fig. S5F), corroborating the presence of a more inflammatory environment in *Trem2*$^{-/-}$ mice treated with anti–PD-1. Together, these data suggest that anti–PD-1 treatment in *Trem2*$^{-/-}$ mice is associated with intestinal subclinical inflammation, in line with a previous report (19).

Considering the expression of TREM2 in macrophages, particularly in colon macrophages (fig. S6A), we investigated whether colon *Trem2*$^{-/-}$ macrophages contributed to subclinical inflammation. Flow cytometry analysis of colonic myeloid cells isolated at day 12 from *Trem2*$^{-/-}$-Sep and *Trem2*$^{+/+}$-Sep mice inoculated with MCA/1956 tumors and treated or not treated with anti–PD-1 revealed no statistically significant differences in the frequency of total myeloid cells, macrophages, monocytes, and neutrophils across all conditions (fig. S6, B and C). To improve the sensitivity of myeloid cell analysis under the same conditions, we performed single-cell RNA sequencing (scRNA-seq) of CD11b^{+} cells sorted from the colon lamina propria (live/CD45^{+}Ly6G^{-}SiglecF^{-}/CD11b^{+}). After quality controls, 16,807 cells were partitioned in 10 clusters (Fig. 4A). The major cell types were manually identified based on cluster markers and previous studies (6, 20). These included (i) macrophages with features of activation and inflammation (cluster 0—*Ccl3*, *Ccl4*, *Rgs1*, and *Atf3*; cluster 2—*H2-Ab*, *H2-M2*, *Il1b*, *Nlrp3*, and *Cd80*); (ii) macrophages with markers of immunosuppression (cluster 1—*Mrc1*, *Stab1*, *Cd163*, *Cd36*, *Fcrls*, *Pf4*, and *F13a1*); (iii) less differentiated macrophages expressing *Ccr2* (cluster 6—*Ccr2*, *Mrc1*, and *Fcrls*); (iv) monocytes (cluster 4—*Ly6i* and *Ccr2*); (v) macrophages with a type I interferon (IFN) signature (cluster 9—*Ifit3* and *Ifit2*); (vi) CD11b^{+} conventional dendritic cells 2 (cDC2) (cluster 3—*Zbtb46* and *Sirpa*) and cDC1 (cluster 8—*Zbtb46* and *Xcr1*); (vii) proliferating monocytes—cDCs (cluster 7—*Mki67*); and (viii) contaminating CD11b-expressing B cells (cluster 5—*Jchain*) (Fig. 4B). TREM2 was expressed in all monocyte-macrophage subsets (clusters 0, 1, 2, 4, 6, and 9 and part of cluster 7) (Fig. 4C). Analysis of cluster abundance

across the four conditions (*Trem2*$^{+/+}$, *Trem2*$^{-/-}$, *Trem2*$^{+/+}$ anti–PD-1, and *Trem2*$^{-/-}$ anti–PD-1) revealed that anti–PD-1 treatment of *Trem2*$^{-/-}$ mice was associated with a limited enrichment of macrophages with immunostimulatory and inflammatory features (clusters 0 and 2), whereas immunosuppressive macrophages (cluster 1) were slightly reduced (Fig. 4A). Moreover, both TNF and a type I IFN signature were induced in cluster 0 (fig. S6D). Conversely, anti–PD-1 treatment in *Trem2*$^{+/+}$ mice was not associated with obvious changes in macrophage populations (Fig. 4A). Negligible differences were also detected in untreated *Trem2*$^{-/-}$-Sep and *Trem2*$^{+/+}$-Sep mice (Fig. 4A). Together, these results suggest that anti–PD-1 treatment in *Trem2*$^{-/-}$ mice biases intestinal macrophages toward a proinflammatorym phenotype that may affect the colonic environment together with the expansion of *R. gnavus*.

Next, we examined whether T cells isolated from the colon of tumor-bearing *Trem2*$^{-/-}$ mice treated with anti–PD-1 also exhibited a proinflammatory profile. Flow cytometric analysis documented increased frequency of total CD3$^+$ T cells in the colon lamina propria of *Trem2*$^{-/-}$-Sep mice compared with *Trem2*$^{+/+}$-Sep controls at day 12 after tumor injection (Fig. 4D); this difference was abrogated in co-housed mice. The frequency of colonic CD4$^+$ and CD8$^+$ T cells, as well as PD-1$^+$ T cells, was similar among all experimental groups (fig. S6E); the proportions of T cells in mesenteric lymph nodes (mLNs) were also comparable (fig. S6F). In anti–PD-1–treated tumor-bearing *Trem2*$^{-/-}$ mice, higher frequencies of colonic TNF-producing CD4$^+$ T cells were observed compared with anti–PD-1–treated *Trem2*$^{+/+}$ mice and all untreated mice (Fig. 4E). We conclude that microbiota alteration in anti–PD-1–treated *Trem2*$^{-/-}$ mice is associated with an expansion of TNF-producing CD4$^+$ T cells in the colon.

Microbiota derived from TREM2-deficient mice promotes gut T cell migration to the tumor bed

We determined how remodeling of the gut microbiota and immune landscapes may affect the efficacy of anti–PD-1 in controlling tumor growth at a distant site. We tested the hypothesis that imprinting of T cells by the subclinical inflammation induced by anti–PD-1 treatment in *Trem2*$^{-/-}$ mice can facilitate their migration to the tumor bed. To track gut-imprinted T cells in the MCA/1956 tumor model, we used mice globally expressing Kikume Green-Red (KikGR), a green-to-red photoconvertible fluorescent protein (21, 22). Application of an infrared laser light to surgically exposed colon or mLNs converted cells from KikG$^+$ to KikR$^+$; photoconversion was complete in mLNs (>99%) but partial in the colon (55% to 80%). KikR$^+$ cells were detected in both tumors and dLNs starting from 48 hours up to 4 days after photoconversion and were 31.32 ± 11.30 more enriched in dLNs than tumors (Fig. 5 and fig. S7A). Because the frequency of KikR$^+$ cells in dLNs and tumors was higher after photoconversion in mLNs than in colons, we only applied the laser light to mLNs in all subsequent experiments.

Next, two groups of KikGR mice were reconstituted with mbt-d12 obtained from either *Trem2*$^{+/+}$-Sep or *Trem2*$^{-/-}$-Sep mice inoculated with MCA/1956 and treated with anti–PD-1 (Fig. 5A). After CMT, KikGR mice were inoculated with MCA/1956 at day 0, treated with anti–PD-1 at day 9, exposed to infrared laser light in the mLNs at day 10, treated again with anti–PD-1 at day 12, and euthanized for collection of tumors and tumor dLNs at

day 14 (Fig. 5A). KikR$^+$ and KikG$^+$ T cells were sorted from tumor dLNs and tested for intracellular cytokine content after in vitro stimulation with phorbol 12-myristate 13-acetate (PMA)–ionomycin. KikR$^+$ CD4$^+$ T cells derived from mice reconstituted with mbt-d12 of *Trem2*$^{-/-}$-Sep mice produced significantly more TNF than KikG$^+$ cells from the same mice and KikR$^+$ CD4$^+$ T cells from mice that had received mbt-d12 of *Trem2*$^{+/+}$-Sep mice (Fig. 5B). No statistically significant differences were observed in KikR$^+$ CD8$^+$ T cells (fig. S7B). Thus, gut CD4$^+$ T cells imprinted by the mild inflammatory environment in anti–PD-1–treated TREM2-deficient mice are predisposed to produce TNF upon reaching the tumor dLNs. Additionally, the frequency of KikR$^+$ T cells in tumor dLNs was significantly higher in KikGR mice reconstituted with mbt-d12 from *Trem2*$^{-/-}$-Sep mice than in counterparts receiving mbt-d12 from *Trem2*$^{+/+}$-Sep mice, although the frequencies of KikR$^+$ T cells in tumors, contralateral LNs, and spleens were similar (Fig. 5, C and D). Notably, the frequency of KikG$^+$ T cells in tumor dLNs was also higher in KikGR mice transplanted with mbt-d12 from *Trem2*$^{-/-}$-Sep mice (Fig. 5E), suggesting that mbt-d12 from *Trem2*$^{-/-}$-Sep mice promoted not only T cell migration from the gut but also either in situ expansion or recruitment from other sites. Hence, apart from its local effect, mbt-d12 may also exert a systemic influence, further affecting T cell migration into the tumor bed.

Oral gavage of *R. gnavus* enhances tumor response to anti–PD-1

From a translational perspective, we aimed to directly investigate the specific impact of *R. gnavus* on the efficacy of anti–PD-1, irrespective of TREM2 deficiency. To determine whether the enrichment of *R. gnavus* observed in *Trem2*$^{-/-}$-Sep mice played a causal role in improving tumor growth control, we administered *R. gnavus* [1.5×10^6 colony-forming units (CFU) per mouse] to wild-type mice by daily oral gavage for 1 week starting at day 10 after subcutaneous tumor inoculation, in addition to anti–PD-1, and monitored tumor growth (Fig. 6A). Wild-type mice that received *R. gnavus* controlled tumor growth substantially better than their counterparts (Fig. 6B). In control experiments, *Clostridium scindens* was chosen as the closest taxon assigned to *R. gnavus* V4–16*S* sequence, but its administration did not affect tumor growth (fig. S8A). Moreover, heat inactivation (100°C) of *R. gnavus* impaired the capacity of the bacterium to provide protection, suggesting that the exposure to the live microorganism or certain heat-sensitive components are necessary to drive tumor control (fig. S8B).

To assess the influence of *R. gnavus* on the tumor's immune environment, we conducted scRNA-seq on sorted CD45$^+$ cells isolated from MCA/1956 tumors in mice that received anti–PD-1 treatment and were either gavaged with *R. gnavus* or received a vehicle. We obtained a total of 25,095 cells from the two groups after quality controls, which were then projected onto a uniform manifold approximation and projection (UMAP) encompassing five major populations (Fig. 6C). Macrophages, monocytes, and dendritic cells expressing *Fcgr1*, *Ly6c2*, and *Zbtb46*, respectively, encompassed clusters 0, 1, 2, 5, 9, 11, 14, and 18. T cells comprised TCRαβ+ CD4$^+$ (clusters 6 and 8—*Trac* and *Cd4*) and CD8$^+$ (clusters 4 and 12 and a portion of cluster 6—*Trac* and *Cd8*) T cells, as well as a small proportion of TCRγδ+ T cells (cluster 15—*Trdc*). NK cells corresponded to clusters 3 and 7, with cluster 3 cells showing chemokine production (C*cl5*) and cluster 7 exhibiting cytotoxicity (*Gzmc*). Neutrophils corresponded to cluster 10 (*S100a9*), whereas B cells were found in cluster 13

(*Cd19*) (Fig. 6, C and D). After exposure to *R. gnavus*, we observed substantial remodeling of the macrophage landscape and an increased frequency in all TCRαβ+ $CD4^+$ and $CD8^+$ T cell clusters, including activated $CD8^+$ T cells (cluster 4), resting $CD4^+$ and $CD8^+$ T cells (cluster 6), and cycling $CD8^+$ T cells (cluster 12). Regulatory T cells (cluster 8) remained unchanged, whereas TCRγδ+ T cells (cluster 15) showed a slight decrease (Fig. 6, E to H).

To further examine the complexity of macrophage changes, we reclustered myeloid cell populations, resulting in 14 clusters (Fig. 7A and fig. S9, A and B). Notably, in *R. gnavus*–treated mice, clusters 0 (Il1r2 Macs) and 3 ($Trem2^{high}$ Macs) decreased in size, whereas clusters 2 (Cd300e Macs), 4 (Fabp5 Macs), and 5 (Tmem176 Macs) expanded (Fig. 7, B and C, and fig. S9C). Cluster 0 showed heterogeneous features: It was enriched for IL-1 family molecules, such as *Il1r2* and *Il1b*, with the latter being associated with pathogenic inflammation in cancer (23). At the same time, cluster 0 displayed immunostimulatory properties, as indicated by high *Cxcl9* expression (Fig. 7, B and C, and fig. S9A). The impact of *R. gnavus* treatment on the macrophage compartment was particularly evident in changes to the relative abundance of clusters 3 and 4. Both of these clusters expressed markers associated with immunosuppression, such as *Trem2*, *Cx3cr1*, *Arg1*, *Stab1*, and *Mrc1*. However, cluster 3 ($Trem2^{high}$ Macs), which had higher expression of immunosuppressive molecules like *Trem2*, *Cx3cr1*, *Spp1*, *Fn1*, and *Ldha*, was decreased in response to *R. gnavus*. In contrast, cluster 4 (Fabp5 Macs), with higher expression of inflammatory molecules such as *Ccl5*, increased after *R. gnavus* treatment (fig. S9D). Furthermore, *R. gnavus* treatment led to reduced expression of the TGFβ receptor *Tgfbr1* ($P = 0.0286$), whereas the expression of the IFN-γ receptor *Ifngr1* trended toward an increase at least in one macrophage population (cluster 5, $P = 0.0571$) (Fig. 7D). We then generated a manually curated module based on immunosuppressive genes from clusters 3 and 4, which included *Trem2*, *Cx3cr1*, *Arg1*, *Stab1*, *Mrc1*, *Fn1*, and *Ldha*. We projected this module onto the UMAPs of both groups. This signature was enriched in the control group ($P = 0.000186$) when compared with *R. gnavus*–treated mice (Fig. 7E).

We further examined the immune cell infiltration in tumors, mLNs, and colons in controls and *R. gnavus*–treated mice by flow cytometry. We observed that *R. gnavus* treatment induced the enrichment of $MHCII^+$ macrophages, confirming the enrichment of less suppressive myeloid cells in the tumors (Fig. 7F and fig. S10A). We also observed enrichment of migratory conventional dendritic cells (cDCs) and total T cells in mLNs (Fig. 7G and fig. S10B), as well as macrophages and activated T cells in the colon after *R. gnavus* exposure (Fig. 7H), corroborating that *R. gnavus* also drives immunechanges in the gut.

DISCUSSION

We previously found that deficiency of TREM2 amplifies the antitumor efficacy of anti–PD-1 treatment (6). Here, our study demonstrates that this amplification depends on a complex interaction among T cells, TREM2-deficient intestinal macrophages, and intestinal microbiota that creates a subclinical inflammatory environment in the intestine. We believe that it is unlikely that TREM2 deficiency alone is sufficient to induce a proinflammatory polarization of macrophages and the *R. gnavus* expansion, because macrophage signatures

and *R. gnavus* abundance were similar in *Trem2*$^{-/-}$ and *Trem2*$^{+/+}$ mice before anti–PD-1 treatment. We envision that anti–PD-1 activates CD4^{+} T cells in the gut, which engages macrophages through cell surface molecules, such as CD40L, and/or proinflammatory cytokines, such as IFN-γ (24).

Previous work showed that TREM2 attenuates Toll-like receptor signaling, specifically mitogen-activated protein kinase (MAPK) activation (25, 26). Thus, TREM2 deficiency may lead to unhindered macrophage responses to both T cell– and microbial-induced stimuli. Such response might generate a subclinical inflammatory and/or hypoxic state that facilitates the expansion of the anaerobe *R. gnavus*, among other species. This phenomenon mirrors observations in Crohn's disease, where *R. gnavus* colonizing the intestinal mucosal surface blooms during flare-ups of symptoms (18). The specific effect of TREM2 deletion and PD-1 blockade on the gut permeability and integrity, which might enhance the subclinical inflammation state, as well as the mechanism by which *R. gnavus* promotes antitumor responses at a distant site, will require further analysis. *R. gnavus* produces glucorhamnan, a polysaccharide that stimulates the production of TNF by cDCs through TLR4 in vitro (18). Glucorhamnan or other bacterial components that elicit proinflammatory responses may induce TNF-producing T cells and inflammatory macrophages. Moreover, *R. gnavus*–derived metabolites might act locally in the gut environment to promote T cell activation and migration and systemically to directly facilitate the antitumor immune response at distant sites.

Previous analyses of the fecal microbiota delineated the relative abundance of certain bacteria, including *R. gnavus*, in the intestines of mice and patients with cancer responding to PD–1 blockade and showed a causal relationship (10, 11, 27). Our results extend these studies, suggesting that the enrichment of microbiota species associated with heightened response to anti–PD-1 therapy is also influenced by intestinal macrophages. Notably, anti-TREM2 treatment, although enhancing anti–PD-1 control of tumor growth similar to TREM2 deficiency, was not associated with an enrichment of *R. gnavus*. Yet, anti-TREM2 treatment did induce significant changes in the microbiota communities compared with mice treated with a control mAb. These data suggest that the contribution of the microbiome to the efficacy of anti–PD-1 in TREM2 deficiency or blockade does not always depend on *R. gnavus* but might potentially rely on the expansion of different species that enact mechanisms similar to those of *R. gnavus*. Because the abundance of *R. gnavus* in the intestine is relatively low, the impact of these species may depend on their relative abundance before antibody treatment. It will be important to validate this concept in the human population by searching for correlations among responsiveness to anti–PD-1, enrichment of certain microbiota species, and macrophage responsiveness to environmental stimuli. In light of the ongoing clinical trial (NCT04691375), it will be informative to evaluate the effect of TREM2 and PD-1 blockade on gut microbial composition and any relationship to the response to treatment.

MATERIALS AND METHODS

Study design

The goal of this study was to evaluate the link between the gut microbiota and the antitumor effect of TREM2 deletion after anti–PD-1 treatment. We used the syngeneic sarcoma tumor cell line (MCA/1956) that we subcutaneously implanted into *Trem2*$^{+/+}$ and *Trem2*$^{-/-}$ B6 mice. We used different housing conditions to evaluate the effect of the microbiota on anti–PD-1 response. To further corroborate the impact of *Trem2*$^{-/-}$-associated species on the response to anti–PD-1, we performed microbiota transplantation experiments and treated mice with different combinations of antibiotics. We identified the bacterial species associated with TREM2 deficiency through V4–16*S* rRNA sequencing analysis; among those, *R. gnavus* was enriched in anti–PD-1 responder groups. To track the migration of gut-imprinted T cells into the tumor bed, we performed CMT in KikGR mice. We photoconverted the mLNs and analyzed dLNs, tumors, and spleens. To examine the downstream effect of *R. gnavus* on the antitumor immune response, we orally gavaged wild-type (WT) mice with the American Type Culture Collection (ATCC) *R. gnavus* strain. For all experiments, we monitored tumor growth and analyzed the percentage and functions of immune cells in tumors, dLNs, colons, and mLNs by flow cytometry and scRNA-seq. Mice were used for tumor growth experiments and harvesting of mouse tissue, with approved humane end points to terminate in vivo experiments. Sample size was determined by preliminary experiments. For 16*S* and *R. gnavus* gavage experiments, groups were randomized before treatment. Animals that failed to develop tumors were excluded from the analysis. The number of mice and statistical methods used are described in the figure legends.

Animals

All mice used in this study were bred under specific pathogen–free conditions at Washington University School of Medicine animal facility. Mice within experiments were age- and sex-matched, and both sexes were used. Pregnant mothers of different genotypes were co-housed, and litters were cross-fostered, to avoid a potential effect driven by the maternal microbiota. All mice were bred in the same room (SRF-E-228) and were transferred and kept in the same room for experiments (CSRB-742D). All animals consumed a standard polysaccharide-rich mouse chow ad libitum (PicoLab Rodent Diet 20). All mice were housed in standard LD 12:12 conditions (light on from 6:00 a.m. to 6:00 p.m.). Housing conditions before and after weaning and during the experiments are specified in the Results section of the text. Mice from different genotypes were either co-housed from birth and kept co-housed or separated during the experiment (the day of tumor injection). Mice used for the experiment with anti-TREM2 were purchased from the Jackson Laboratory (C57BL/6J). Mice used in this study include WT C57BL/6J, *Trem2*$^{-/-}$, and KikGR [Tg(CAG-KikGR)33Hadj/J—Jax 013753]. KikGR mice were transferred to us by G. Randolph (Washington University School of Medicine). Mice did not undergo any procedures before their stated use. Mice were humanely euthanized at different time points, as indicated. All animals were backcrossed until at least >98% C57BL/6J confirmed by genotype wide microsatellite typing. For tumor models, animals were injected at 8 to 10 weeks of age. All studies performed on mice were done in accordance with the Institutional Animal Care and

Use Committee at Washington University in St. Louis, which approved all protocols used in this study (protocol nos. 19–0981, 22–0433, and 22–0274).

Tumor models

The MCA-induced sarcoma cell line (MCA/1956) was generated in female C57BL/6 WT mice in R.D.S's laboratory. Cell batches were frozen as low-passage tumor cells and injected after a maximum of three passages. Mice were shaved on the flank, and MCA/1956 cells were injected subcutaneously [10^6 cells per mouse in 100 μl of phosphate-buffered saline (PBS)]. Mice were monitored every day, and tumors were measured by caliper every other day. Mice were euthanized on the indicated days or when tumors reached 1.5 cm in diameter.

Flow cytometry

Single-cell suspensions were prepared from the collected tissues upon sacrifice. Tumors were minced and digested with collagenase IV (Sigma) for 30 min at 37°C. Cells were filtered through 70-μm strainers, washed with PBS, and stained for flow cytometry. Lymph nodes were collected and mashed on a 70-μm strainer. Small intestine or colon were collected, flushed with HBSS to remove luminal contents, and opened lengthwise. Peyer's patches were removed. The tissue was gently agitated for 20 min in HBSS with Hepes, BCS, and EDTA. The tissue was rinsed and agitated for a second round of 20 min. After rinsing, the tissue was digested with collagenase IV (Sigma) in complete RPMI (Gibco) for 40 min at 37°C under agitation, as previously described (28). Digested tissue was filtered through a 100-μm strainer, collected into a 50-ml tube, and washed. The following antibodies were used: CD45-AlexaFluor700 or -BUV563 (clone 30-F11); CD11b-PerCPCy5.5, -PECy7, -APC, or -BV421 (clone M1/70); I-A/I-E-BV650 or -BUV805 (clone M5/114.15.2); Ly6C-BV421, -APC, -PerCPCy5.5, or -PE (clone HK1.4); Ly6G-AlexaFluor700 or -APC (clone 1A8); CD64-APC or -BV605 (clone X54–5/7.1); TCRβ-PE (clone H57–597); CD8-BV785 (clone 53–6.7); CD4-PECF594 (clone RM4–5); PD-1-FITC or -APC (clone J43); IFN-γ–APC (clone XMG1.2); TNFa-eFluor 450 (clone MP6-XT22); XCR1-BV605 (ZET); LAG3-PE-Cy7 (C9B7W); TCRgd-BV421 (GL3); CD11c-APC/Cy7 (N418); and FoxP3-AF647 (clone 150D). For cell hashing, the following hashtag antibodies were used: Total-Seq-B0301, B0302, B303, and B304 (clone M1/42; 30-F11). Cells were incubated with Fc block before staining. Cell viability was determined by Aqua LIVE/Dead-405 nm staining (Invitrogen); negative cells were considered viable. Foxp3/Transcription Factor Staining Buffer Set (eBioscience) was used for intracellular staining. Cells were analyzed on BD FACSymphony (BD Bioscience). An AriaII (BD Bioscience) was used for sorting. Data were analyzed with FlowJo software (Treestar).

In vivo treatments

Mice were treated intraperitoneally with anti–PD-1 antibody (200 μg per mouse, clone RMP1–14, Leinco P372) every 3 days, starting at day 9 after tumor injection, as specified above. Anti-TREM2 (178) and control (135.5) antibody (200 μg per mouse) were produced in our laboratory as previously described (6) and were given intraperitoneally every 5 days, starting at day 2 after tumor injection.

T cell stimulation

Single-cell suspensions were prepared from tumors upon sacrifice and leukocytes were enriched with a PercollTM (GE Healthcare) gradient. Obtained cells were cultured in complete RPMI with or without PMA (10^{-7} M, Sigma)–ionomycin (500 ng/ml, Sigma) and Protein Transport Inhibitor Cocktail (eBioscience, 500×) for 4 hours. Cells were collected and stained for flow cytometry analysis.

Real-time PCR

Total RNA was extracted from snap-frozen tissue using the RNeasy Mini Kit (Qiagen Inc.), following the supplier's instructions. RNA was converted to cDNA using the iScript cDNA Synthesis Kit (Bio-Rad), and PCR was performed using iTaq Universal SYBR Green Supermix (Bio-Rad). Gene expression analysis was normalized using the $2^{-\Delta\Delta Ct}$ method with Gapdh as a reference gene. Primers are listed in table S1.

RNA-seq and analysis

Colonic RNA was extracted using an RNeasy mini kit according to the manufacturer's protocol (QIAGEN). Total RNA integrity was determined using Agilent Bioanalyzer or 4200 Tapestation. Library preparation was performed with 5 to 10 μg of total RNA with a Bioanalyzer RIN score greater than 8.0. Ribosomal RNA was removed by poly-A selection using Oligo-dT beads (mRNA Direct kit, Life Technologies). mRNA was then fragmented in reverse transcriptase buffer and heated to 94°C for 8 min. mRNA was reverse-transcribed to yield cDNA using SuperScript III RT enzyme (Life Technologies, per the manufacturer's instructions) and random hexamers. A second strand reaction was performed to yield ds-cDNA. cDNA was blunt ended, had an A base added to the 3′ ends, and then had Illumina sequencing adapters ligated to the ends. Ligated fragments were then amplified for 12 to 15 cycles using primers incorporating unique dual index tags. Fragments were sequenced on an Illumina NovaSeq-6000 using paired-end reads extending 150 bases. RNA-seq reads were then aligned and quantitated to the Ensembl release 101 primary assembly with an Illumina DRAGEN Bio-IT on-premise server running version 4.0.3–8 software. Read counts were used as input and normalized using built-in algorithms in DESeq2 (1.38.3). Pairwise comparisons among the four conditions were done on all genes. The resulting P values were adjusted using Benjamini and Hochberg's approach for controlling the false discovery rate. Genes with an adjusted $P < 0.05$ were assigned as differentially expressed. For pathway enrichment analysis, gene set enrichment analysis (GSEA) was performed using the hallmark pathways from the Molecular Signature Database.

Single-cell RNA sequencing

Sorted cells from the colon lamina propria were washed in PBS + 0.04% BSA at a final concentration of ~1000 cells/μl (Fig. 4). Cells were extracted from tumor (Fig. 6), and before sorting, each sample was labeled with a unique hashtag antibody (TotalSeq B). Sorted cells were resuspended in PBS with 0.04% BSA at a final concentration of approximately 1200 cells/μl, and samples were pooled and loaded on a 10x Genomics Chromium Single-Cell Controller at the McDonnell Genome Institute in Washington University in St. Louis. The 10x Genomics Next GEM Single-Cell 3′ Reagents Kit was used for library generation on

the 10x Genomics platform. This process used the Chromium Next GEM Single Cell 3′ Kit v3.1 (16 reactions), Chromium Next GEM Chip G Single Cell Kit (48 reactions), and Dual Index Kit TT Set A (96 reactions). In brief, up to 23,000 cells were partitioned into nanoliter gel-bead-in-emulsion (GEM) droplets, each containing retro-transcriptase reaction mix. Single-cell cDNA received a unique 12-nucleotide barcode and a unique molecular identifier (UMI). Subsequently, GEM cDNA underwent 11 cycles of amplification before purification using SPRIselect beads. The generation of gene-expression (GEX) and hashtag-oligo (HTO) libraries followed the recommendations outlined in the 10x Genomics Chromium Single-Cell 3′ Reagent Kits User Guide (v3.1 Chemistry Dual Index), with modifications to PCR cycles based on the calculated cDNA concentration. The concentration of each library was determined using qPCR with the KAPA library Quantification Kit following the manufacturer's protocol (KAPA Biosys tems/Roche). The sequencing of normalized cDNA libraries was performed on a NovaSeq6000 S4 Flow Cell using the XP workflow and a 28 × 10 × 10 × 150 sequencing recipe as per the manufacturer's protocol (Illumina). A median sequencing depth of 50,000 and 5000 reads per cell was targeted for the GEX and HTO library, respectively. For gene expression comparisons (Fig. 7, D and E), we performed a pseudobulk analysis and extracted log-transformed counts. For Fig. 7E, we then performed DESeq2 analysis and pathway enrichment analysis for selected genes.

scRNA-seq analysis

The Cell Ranger Software Suite (v6.0.0) by 10x Genomics was used for sample demultiplexing, barcode processing, and single-cell counting. Subsequent analysis was conducted using the Seurat package (v4.1.1) in R. The HTODemux function from the Seurat package was used for demultiplexing. Quality control entailed the removal of cells with mitochondrial content exceeding 5%, as well as those containing fewer than 1000 or more than 7000 genes per cell. Raw UMIs in each cell were both scaled and normalized via the SCTransform algorithm, regressing out unwanted source of variation arising from the percentage of mitochondrial genes. Highly variable genes were identified and selected for PCA reduction of high-dimensional data. To reduce dimensionality, the RunUMAP, Find-Neighbors, and FindClusters functions were used including the top 20 principal components. All visualization was done with BioTuring version 3 and BBrowserX (BioTuring).

In situ photoconversion

mLN photoconversion was performed as previously reported (22). In brief, mice were anesthetized with 2% isoflurane during the procedure. mLNs and colons were exposed by an abdominal wall incision. Opaque, nonreflective material was used to shield the mouse from light exposure, except at the desired site. Photoconversion was performed using a low-power 80-mW LED-violet laser (Laser-land) in three cycles of 10 s powered on followed by 30 s powered off, keeping the light source approximately 2 cm away from the tissue. mLNs were photoconverted with three consecutive spots, comprising the whole mLN chain. Colons were photoconverted with six consecutives spots in the proximal colon, labeling approximately 3 cm of colon length. Next, mice were sutured and allowed to recover from anesthesia on a heating pad until responsive. After surgery, mice were given long-acting buprenorphine for analgesia. $KikR^+$ cells present outside the photoconverted area were quantified by flow cytometry to establish emigrated cells.

Antibiotic treatment

Mice were treated for 6 weeks with the following antibiotics in their drinking water: ampicillin (Sigma-Aldrich) 1 g/liter, vancomycin (Sigma-Aldrich) 0.5 g/liter, neomycin (Sigma-Aldrich) 1 g/liter, and metronidazole (Sigma-Aldrich) 1 g/liter, together (VNAM) or separately as indicated. Grape Kool-Aid (Kraft Foods; 20 g/liter) was used as vehicle. In the microbiota transplantation experiment, recipient mice were treated for 3 weeks with the VNAM antibiotic cocktail before recolonization.

Microbiota transfer

Trem2$^{+/+}$ and *Trem2*$^{-/-}$ recipient mice (8 weeks old) were treated for 3 weeks with the following antibiotics in the drinking water: ampicillin (Sigma-Aldrich) 1 g/liter, vancomycin (Sigma-Aldrich) 0.5 g/liter, neomycin (Sigma-Aldrich) 1 g/liter, and metronidazole (Sigma-Aldrich) 1 g/liter. Two days after the antibiotic treatment was stopped, mice were gavaged with microbiota harvested from the ceca of different donors as indicated (n = 3 mice per donor genotype/treatment group). Briefly, each donor microbiota sample was weighed and brought into the Coy chamber. Three animals were euthanized for each donor genotype (*Trem2*$^{+/+}$ or *Trem2*$^{-/-}$) at day 0 (before tumor injection; referred to as mbt-d0) or at day 12 (48 hours after the first anti–PD-1 injection; referred to as mbt-d12). Cecal contents isolated from the three animals belonging to the same donor genotype/treatment group were combined and diluted 1:10 (wt/vol) with reduced PBS (PBS/0.05% L-cysteine–HCl) in 50-ml conical plastic tubes. Tubes were gently vortexed, and the resulting slurry was passed through a 100-μm–pore diameter nylon cell strainer (BD Falcon). The clarified cecal sample was then combined with an equal volume of a solution of PBS/0.05% L-cysteine–HCl/30% glycerol and aliquoted into 1.8-ml glass vials (E-Z vials, Wheaton). Tubes were crimped with covers containing a polytetrafluoroethylene (PTFE)/gray butyl liner (Wheaton) and stored at −80°C until use (29). Each recipient mouse received 150 μl of the clarified cecal content one time 2 days after the end of the antibiotic treatment, as described above.

V4–16*S* rRNA amplicon sequencing

DNA was isolated from mouse fecal samples by bead beating in phenol:chloroform and purified on QiaQuick plates (QIAGEN). PCR amplification of V4 of bacterial 16*S* rRNA genes present in fecal samples was performed using published primers and cycling conditions (29). Amplicons were sequenced using an Illumina MiSeq instrument (2 × 250 nucleotide reads; 970,038 ± 75,587 reads per sample). Amplicon sequences were oriented, trimmed of adaptor and primer sequences, and paired using the bbtools (37.02) software package (https://sourceforge.net/projects/bbmap/“bbduk.sh” and “repair.sh” tools). DADA2 (1.8.0) was used to remove chimeric sequences and to identify ASVs (30). Representative sequences for ASVs were then used for taxonomic profiling using the following multi-taxonomic assignment (MTA) approach. Each representative sequence was aligned using NCBI BLAST toolkit version 2.10.0 to the 16*S* rRNA gene reference database compiled by joining unique sequences from two databases: Ribosomal Database Project version 11.5 and the NCBI 16*S* ribosomal RNA Project.

In vivo treatment with selected bacterial species

R. gnavus VPI c7–9 (ATCC; ref. no. 29149) was grown at 37°C in Wilkins-Chalgren anaerobe broth (Oxoid; ref. no. CM0643) in a Coy chamber (atmosphere: 75% N_2, 20% CO_2, and 5% H_2) without shaking. The overnight *R. gnavus* culture was mixed with filter-sterilized PBS solution containing 30% glycerol and 0.05% cysteine in a 1:1 (v/v) ratio (freezing medium). The resulting bacterial stocks were preserved at −80°C before experiments. The number of viable *R. gnavus* in the stocks was quantified by the CFU counting method. *C. scindens* was used as a control because it represents the next closest taxon assigned to the V4–16*S* sequence associated to *R. gnavus* against the NCBI 16*S* rDNA database. *C. scindens* was obtained from ATCC (35704) and was grown and prepared for gavage as specified above for *R. gnavus*. For the heat inactivation experiment, *R. gnavus* was kept at 100°C for 1 hour before freezing. Mice were injected with MCA/1956 tumors and treated with anti–PD-1 as previously described. Each mouse was treated with 150 μl of the stock via oral gavage, containing 1.5×10^7 viable *R. gnavus*. The oral gavage with the bacterium was performed daily for 5 days, starting at day 7 after tumor injection. Controls were treated with a vehicle (freezing medium). Anti–PD-1 was injected starting at day 9, and tumors were monitored daily as specified.

Statistical analysis

Data are shown as mean ± SEM. Two-way analysis of variance (ANOVA) was used to model data generated from factorial design with the combination of two factors, and two-way ANOVA for repeated-measures was used to model longitudinal tumor growth between treatments followed by post hoc comparisons on treatment difference at time points (Tukey's or Šidák's multiple comparisons test was used as indicated in figure legends). The Mann-Whitney *U* test was used to compare two groups. Statistics were calculated with GraphPad Prism 6 (GraphPad Software). PCoAs were performed using the R packages "ape" (31) and "vegan" (32). Indicator species analysis was conducted using the package "indicspecies" (33). PERMANOVA analyses were performed using 1000 permutations to estimate the statistical significance (*P* value) of the comparison between the groups in the PCA. For gene expression comparison analysis (Fig. 7D), Mann-Whitney *U* test was used for log-transformed counts.

Supplementary Material

Refer to Web version on PubMed Central for supplementary material.

Acknowledgments:

We thank the Genome Technology Access Center at the McDonnell Genome Institute at Washington University for scRNA-seq on the 10× platform. We thank G. J. Randolph for helpful discussions and for sharing reagents. We thank E. Lantelme, D. Brinja, P. Akitani, and the Pathology and Immunology Flow Cytometry Core for cell sorting. We thank F. Changxu for valuable technical support.

Funding:

M. Colonna was supported by the National Institutes of Health (R01 CA262684). M.M. was a recipient of the Cancer Research Institute-Lloyd J. Old Memorial Fellowship in Tumor Immunology and was supported by the American Gastroenterological Association (AGA2023-13-06). R.S.C. and E.J.O. were supported by the National Institutes of Health (R01 DK119147). R.S.C. was supported by the Crohn's and Colitis Foundation (#938100). The

Genome Technology Access Center at the McDonnell Genome Institute at Washington University is supported by the Washington University Institute of Clinical and Translational Sciences grant UL1TR002345 from the National Center for Advancing Translational Sciences (NCATS) of the NIH.

Data and materials availability:

Single-cell and bulk RNA sequencing data have been deposited in GEO under accession number GSE262811. 16*S* rRNA sequencing data have been deposited in BioProject under accession number PRJNA1091180. Tabulated data underlying the figures are provided in data file S7. All other data needed to evaluate the conclusions in the paper are present in the paper or the Supplementary Materials.

REFERENCES AND NOTES

1. Leach DR, Krummel MF, Allison JP, Enhancement of antitumor immunity by CTLA-4 blockade. Science 271, 1734–1736 (1996).
2. Freeman GJ, Long AJ, Iwai Y, Bourque K, Chernova T, Nishimura H, Fitz LJ, Malenkovich N, Okazaki T, Byrne MC, Horton HF, Fouser L, Carter L, Ling V, Bowman MR, Carreno BM, Collins M, Wood CR, Honjo T, Engagement of the PD-1 immunoinhibitory receptor by a novel B7 family member leads to negative regulation of lymphocyte activation. J. Exp. Med. 192, 1027–1034 (2000).
3. Sharma P, Siddiqui BA, Anandhan S, Yadav SS, Subudhi SK, Gao J, Goswami S, Allison JP, The next decade of immune checkpoint therapy. Cancer Discov. 11, 838–857 (2021).
4. Mantovani A, Allavena P, Marchesi F, Garlanda C, Macrophages as tools and targets in cancer therapy. Nat. Rev. Drug Discov. 21, 799–820 (2022).
5. Molgora M, Colonna M, Turning enemies into allies-reprogramming tumor-associated macrophages for cancer therapy. Med 2, 666–681 (2021).
6. Molgora M, Esaulova E, Vermi W, Hou J, Chen Y, Luo J, Brioschi S, Bugatti M, Omodei AS, Ricci B, Fronick C, Panda SK, Takeuchi Y, Gubin MM, Faccio R, Cella M, Gilfillan S, Unanue ER, Artyomov MN, Schreiber RD, Colonna M, TREM2 modulation remodels the tumor myeloid landscape enhancing anti-PD-1 immunotherapy. Cell 182, 886–900.e17 (2020).
7. Katzenelenbogen Y, Sheban F, Yalin A, Yofe I, Svetlichnyy D, Jaitin DA, Bornstein C, Moshe A, Keren-Shaul H, Cohen M, Wang SY, Li B, David E, Salame TM, Weiner A, Amit I, Coupled scRNA-seq and intracellular protein activity reveal an immunosuppressive role of TREM2 in cancer. Cell 182, 872–885.e19 (2020).
8. Binnewies M, Pollack JL, Rudolph J, Dash S, Abushawish M, Lee T, Jahchan NS, Canaday P, Lu E, Norng M, Mankikar S, Liu VM, du X, Chen A, Mehta R, Palmer R, Juric V, Liang L, Baker KP, Reyno L, Krummel MF, Streuli M, Sriram V, Targeting TREM2 on tumor-associated macrophages enhances immunotherapy. Cell Rep. 37, 109844 (2021).
9. Timperi E, Gueguen P, Molgora M, Magagna I, Kieffer Y, Lopez-Lastra S, Sirven P, Baudrin LG, Baulande S, Nicolas A, Champenois G, Meseure D, Vincent-Salomon A, Tardivon A, Laas E, Soumelis V, Colonna M, Mechta-Grigoriou F, Amigorena S, Romano E, Lipid-associated macrophages are induced by cancer-associated fibroblasts and mediate immune suppression in breast cancer. Cancer Res. 82, 3291–3306 (2022).
10. Gopalakrishnan V, Spencer CN, Nezi L, Reuben A, Andrews MC, Karpinets TV, Prieto PA, Vicente D, Hoffman K, Wei SC, Cogdill AP, Zhao L, Hudgens CW, Hutchinson DS, Manzo T, Petaccia de Macedo M, Cotechini T, Kumar T, Chen WS, Reddy SM, Szczepaniak Sloane R, Galloway-Pena J, Jiang H, Chen PL, Shpall EJ, Rezvani K, Alousi AM, Chemaly RF, Shelburne S, Vence LM, Okhuysen PC, Jensen VB, Swennes AG, McAllister F, Marcelo Riquelme Sanchez E, Zhang Y, le Chatelier E, Zitvogel L, Pons N, Austin-Breneman JL, Haydu LE, Burton EM, Gardner JM, Sirmans E, Hu J, Lazar AJ, Tsujikawa T, Diab A, Tawbi H, Glitza IC, Hwu WJ, Patel SP, Woodman SE, Amaria RN, Davies MA, Gershenwald JE, Hwu P, Lee JE, Zhang J, Coussens LM, Cooper ZA, Futreal PA, Daniel CR, Ajami NJ, Petrosino JF, Tetzlaff MT, Sharma P, Allison JP, Jenq RR, Wargo JA, Gut microbiome modulates response to anti-PD-1 immunotherapy in melanoma patients. Science 359, 97–103 (2018).

11. Routy B, Le Chatelier E, Derosa L, Duong CPM, Alou MT, Daillère R, Fluckiger A, Messaoudene M, Rauber C, Roberti MP, Fidelle M, Flament C, Poirier-Colame V, Opolon P, Klein C, Iribarren K, Mondragón L, Jacquelot N, Qu B, Ferrere G, Clémenson C, Mezquita L, Masip JR, Naltet C, Brosseau S, Kaderbhai C, Richard C, Rizvi H, Levenez F, Galleron N, Quinquis B, Pons N, Ryffel B, Minard-Colin V, Gonin P, Soria JC, Deutsch E, Loriot Y, Ghiringhelli F, Zalcman G, Goldwasser F, Escudier B, Hellmann MD, Eggermont A, Raoult D, Albiges L, Kroemer G, Zitvogel L, Gut microbiome influences efficacy of PD-1-based immunotherapy against epithelial tumors. Science 359, 91–97 (2018).
12. Sivan A, Corrales L, Hubert N, Williams JB, Aquino-Michaels K, Earley ZM, Benyamin FW, Man Lei Y, Jabri B, Alegre ML, Chang EB, Gajewski TF, Commensal Bifidobacterium promotes antitumor immunity and facilitates anti-PD-L1 efficacy. Science 350, 1084–1089 (2015).
13. Roy S, Trinchieri G, Microbiota: A key orchestrator of cancer therapy. Nat. Rev. Cancer 17, 271–285 (2017).
14. Iida N, Dzutsev A, Stewart CA, Smith L, Bouladoux N, Weingarten RA, Molina DA, Salcedo R, Back T, Cramer S, Dai RM, Kiu H, Cardone M, Naik S, Patri AK, Wang E, Marincola FM, Frank KM, Belkaid Y, Trinchieri G, Goldszmid RS, Commensal bacteria control cancer response to therapy by modulating the tumor microenvironment. Science 342, 967–970 (2013).
15. Davar D, Dzutsev AK, McCulloch JA, Rodrigues RR, Chauvin JM, Morrison RM, Deblasio RN, Menna C, Ding Q, Pagliano O, Zidi B, Zhang S, Badger JH, Vetizou M, Cole AM, Fernandes MR, Prescott S, Costa RGF, Balaji AK, Morgun A, Vujkovic-Cvijin I, Wang H, Borhani AA, Schwartz MB, Dubner HM, Ernst SJ, Rose A, Najjar YG, Belkaid Y, Kirkwood JM, Trinchieri G, Zarour HM, Fecal microbiota transplant overcomes resistance to anti-PD-1 therapy in melanoma patients. Science 371, 595–602 (2021).
16. Baruch EN, Youngster I, Ben-Betzalel G, Ortenberg R, Lahat A, Katz L, Adler K, Dick-Necula D, Raskin S, Bloch N, Rotin D, Anafi L, Avivi C, Melnichenko J, Steinberg-Silman Y, Mamtani R, Harati H, Asher N, Shapira-Frommer R, Brosh-Nissimov T, Eshet Y, Ben-Simon S, Ziv O, Khan MAW, Amit M, Ajami NJ, Barshack I, Schachter J, Wargo JA, Koren O, Markel G, Boursi B, Fecal microbiota transplant promotes response in immunotherapy-refractory melanoma patients. Science 371, 602–609 (2021).
17. Derosa L, Hellmann MD, Spaziano M, Halpenny D, Fidelle M, Rizvi H, Long N, Plodkowski AJ, Arbour KC, Chaft JE, Rouche JA, Zitvogel L, Zalcman G, Albiges L, Escudier B, Routy B, Negative association of antibiotics on clinical activity of immune checkpoint inhibitors in patients with advanced renal cell and non-small-cell lung cancer. Ann. Oncol. 29, 1437–1444 (2018).
18. Henke MT, Kenny DJ, Cassilly CD, Vlamakis H, Xavier RJ, Clardy J, *Ruminococcus gnavus*, a member of the human gut microbiome associated with Crohn's disease, produces an inflammatory polysaccharide. Proc. Natl. Acad. Sci. U.S.A. 116, 12672–12677 (2019).
19. Seno H, Miyoshi H, Brown SL, Geske MJ, Colonna M, Stappenbeck TS, Efficient colonic mucosal wound repair requires Trem2 signaling. Proc. Natl. Acad. Sci. U.S.A. 106, 256–261 (2009).
20. Gubin MM, Esaulova E, Ward JP, Malkova ON, Runci D, Wong P, Noguchi T, Arthur CD, Meng W, Alspach E, Medrano RFV, Fronick C, Fehlings M, Newell EW, Fulton RS, Sheehan KCF, Oh ST, Schreiber RD, Artyomov MN, High-dimensional analysis delineates myeloid and lymphoid compartment remodeling during successful immune-checkpoint cancer therapy. Cell 175, 1014–1030.e19 (2018).
21. Tsutsui H, Karasawa S, Shimizu H, Nukina N, Miyawaki A, Semi-rational engineering of a coral fluorescent protein into an efficient highlighter. EMBO Rep. 6, 233–238 (2005).
22. Czepielewski RS, Erlich EC, Onufer EJ, Young S, Saunders BT, Han YH, Wohltmann M, Wang PL, Kim KW, Kumar S, Hsieh CS, Scallan JP, Yang Y, Zinselmeyer BH, Davis MJ, Randolph GJ, Ileitis-associated tertiary lymphoid organs arise at lymphatic valves and impede mesenteric lymph flow in response to tumor necrosis factor. Immunity 54, 2795–2811.e9 (2021).
23. Caronni N, la Terza F, Vittoria FM, Barbiera G, Mezzanzanica L, Cuzzola V, Barresi S, Pellegatta M, Canevazzi P, Dunsmore G, Leonardi C, Montaldo E, Lusito E, Dugnani E, Citro A, Ng MSF, Schiavo Lena M, Drago D, Andolfo A, Brugiapaglia S, Scagliotti A, Mortellaro A, Corbo V, Liu Z, Mondino A, Dellabona P, Piemonti L, Taveggia C, Doglioni C, Cappello P, Novelli F, Iannacone M, Ng LG, Ginhoux F, Crippa S, Falconi M, Bonini C, Naldini L, Genua M, Ostuni R, IL-1β^{+} macrophages fuel pathogenic inflammation in pancreatic cancer. Nature 623, 415–422 (2023).

24. Guerriero JL, Macrophages: Their untold story in T cell activation and function. Int. Rev. Cell Mol. Biol. 342, 73–93 (2019).

25. Ito H, Hamerman JA, TREM-2, triggering receptor expressed on myeloid cell-2, negatively regulates TLR responses in dendritic cells. Eur. J. Immunol. 42, 176–185 (2012).

26. Turnbull IR, Gilfillan S, Cella M, Aoshi T, Miller M, Piccio L, Hernandez M, Colonna M, Cutting edge: TREM-2 attenuates macrophage activation. J. Immunol. 177, 3520–3524 (2006).

27. McCulloch JA, Davar D, Rodrigues RR, Badger JH, Fang JR, Cole AM, Balaji AK, Vetizou M, Prescott SM, Fernandes MR, Costa RGF, Yuan W, Salcedo R, Bahadiroglu E, Roy S, DeBlasio RN, Morrison RM, Chauvin JM, Ding Q, Zidi B, Lowin A, Chakka S, Gao W, Pagliano O, Ernst SJ, Rose A, Newman NK, Morgun A, Zarour HM, Trinchieri G, Dzutsev AK, Intestinal microbiota signatures of clinical response and immune-related adverse events in melanoma patients treated with anti-PD-1. Nat. Med. 28, 545–556 (2022).

28. Bando JK, Gilfillan S, Song C, McDonald KG, Huang SCC, Newberry RD, Kobayashi Y, Allan DSJ, Carlyle JR, Cella M, Colonna M, The tumor necrosis factor superfamily member RANKL suppresses effector cytokine production in group 3 innate lymphoid cells. Immunity 48, 1208–1219.e4 (2018).

29. Gehrig JL, Venkatesh S, Chang HW, Hibberd MC, Kung VL, Cheng J, Chen RY, Subramanian S, Cowardin CA, Meier MF, O'Donnell D, Talcott M, Spears LD, Semenkovich CF, Henrissat B, Giannone RJ, Hettich RL, Ilkayeva O, Muehlbauer M, Newgard CB, Sawyer C, Head RD, Rodionov DA, Arzamasov AA, Leyn SA, Osterman AL, Hossain MI, Islam M, Choudhury N, Sarker SA, Huq S, Mahmud I, Mostafa I, Mahfuz M, Barratt MJ, Ahmed T, Gordon JI, Effects of microbiota-directed foods in gnotobiotic animals and undernourished children. Science 365, eaau4732 (2019).

30. Callahan BJ, McMurdie PJ, Rosen MJ, Han AW, Johnson AJA, Holmes SP, DADA2: High-resolution sample inference from Illumina amplicon data. Nat. Methods 13, 581–583 (2016).

31. Paradis E, Schliep K, ape 5.0: An environment for modern phylogenetics and evolutionary analyses in R. Bioinformatics 35, 526–528 (2019).

32. Oksanen J, Blanchet F Guillaume, Friendly M, Kindt R, Legendre P, McGlinn D, Minchin PR, O'Hara RB, Simpson GL, Solymos P, Stevens MHH, Szoecs E, Wagner H, vegan: Community Ecology Package 2 (2019); http://CRAN.R-project.org/package=vegan.

33. De Caceres M, Legendre P, Associations between species and groups of sites: Indices and statistical inference. Ecology 90, 3566–3574 (2009).

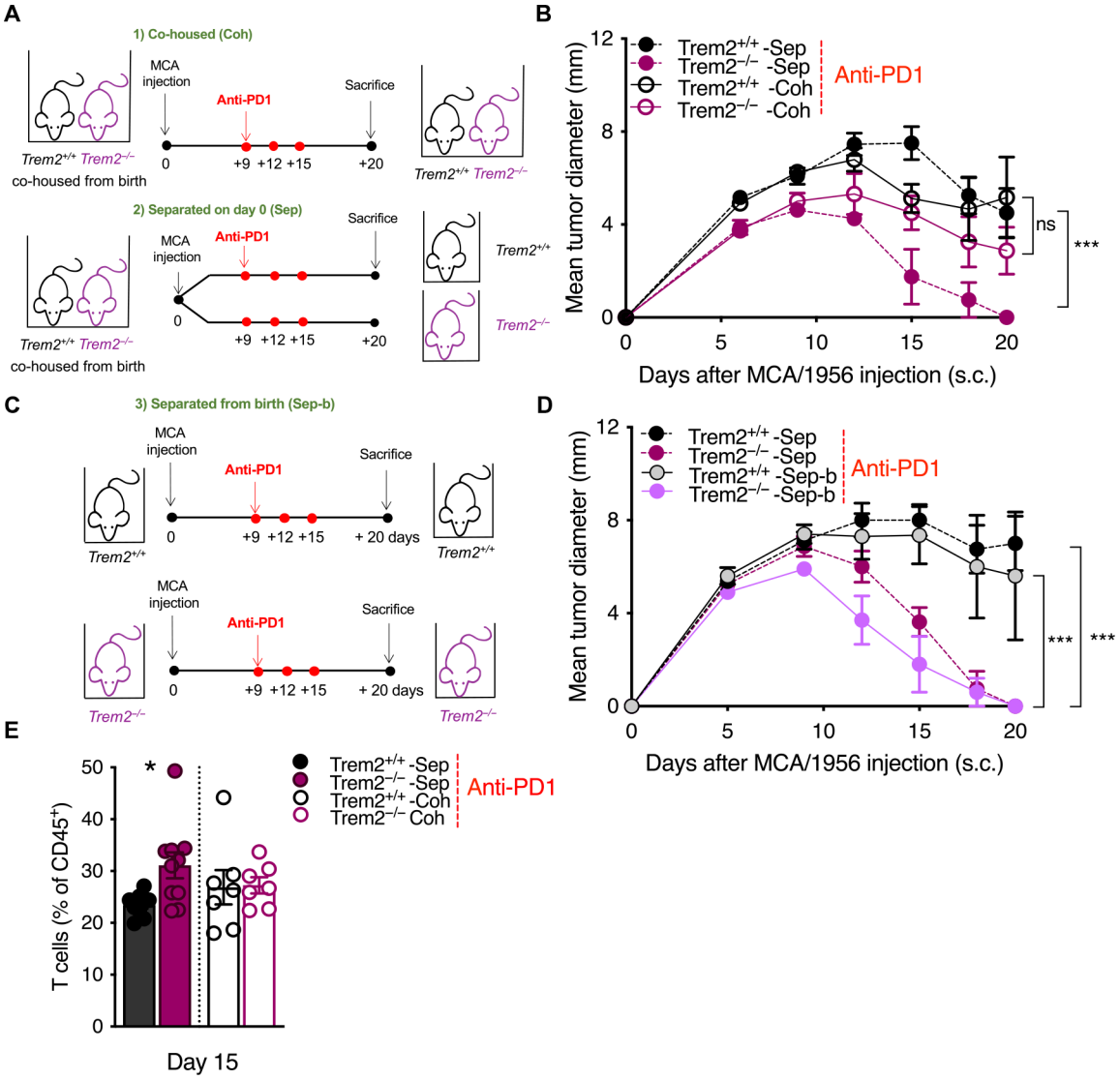

Fig. 1. Co-housing of TREM2-deficient and wild-type mice abolishes the improved tumor response to anti–PD-1 observed in the absence of TREM2.

(**A**) Experimental schemes. Mice were co-housed from birth and kept co-housed during the experiment (Coh) or separated at day 0 (Sep). Pregnant mothers of different genotypes were co-housed and litters were cross-fostered to avoid a potential effect driven by the maternal microbiota. (**B**) MCA/1956 tumor growth in the indicated conditions: wild-type (*Trem2*$^{+/+}$) or TREM2-deficient (*Trem2*$^{-/-}$) Sep Coh. All groups were treated with anti–PD-1 (n = 4 to 6). (**C**) Experimental schemes. Mice were generated from separated breeders and therefore separated at birth (Sep-b). (**D**) MCA/1956 tumor growth in the indicated conditions: *Trem2*$^{+/+}$ or *Trem2*$^{-/-}$ Sep or Sep-b (n = 4 or 5). (E) T cell frequency in the tumor at day 15 after tumor injection in the indicated groups. (B and D) All groups were treated with anti–PD-1. Results are representative of at least two independent experiments and are presented as means ± SEM. Two-way ANOVA followed by post hoc comparisons (Tukey's multiple comparisons test) of time points was used to compare tumor growth across the indicated conditions; statistical significance is indicated for the last time point of

the curve. (E) Mann-Whitney *U* test was used to compare two groups (****P* < 0.001; **P* < 0.05).

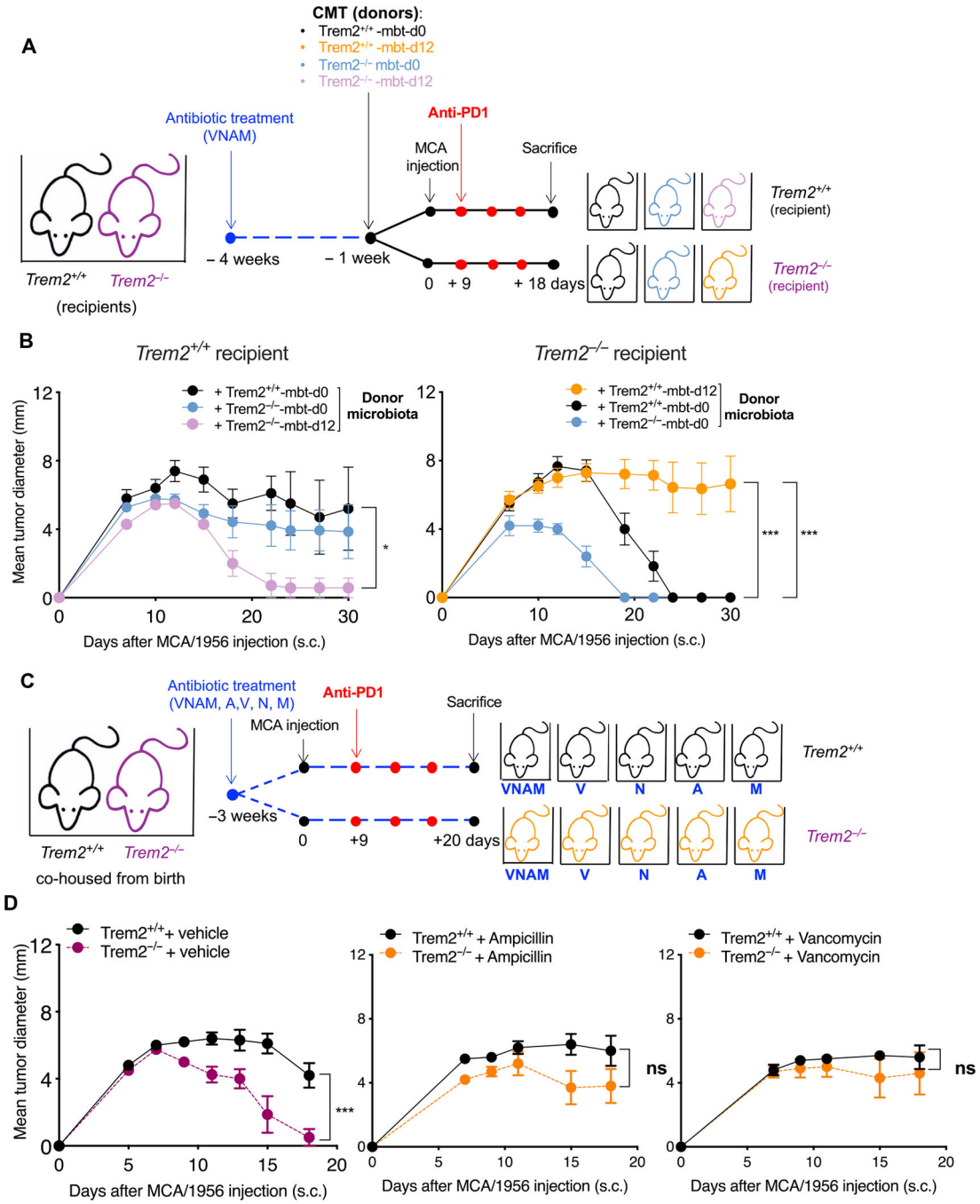

Fig. 2. Gut microbiota affects tumor response to anti–PD-1 in the absence of TREM2.

(**A**) Schematic representation of CMT experiment. *Trem2*$^{+/+}$ and *Trem2*$^{-/-}$ mice were treated with a cocktail of antibiotics (VNAM) for 3 weeks before colonization with cecal contents previously collected from either *Trem2*$^{+/+}$ or *Trem2*$^{-/-}$ at steady state (mbt-d0) or 3 days after the anti–PD-1 injection (mbt-d12). (**B**) MCA/1956 tumor growth curve of *Trem2*$^{+/+}$ mice (left) colonized with cecal contents previously collected from either *Trem2*$^{+/+}$-mbt-d0, *Trem2*$^{-/-}$-mbt-d0, or *Trem2*$^{-/-}$-mbt-d12; tumor growth curve in *Trem2*$^{-/-}$ mice (right) colonized with cecal contents collected from either *Trem2*$^{+/+}$-mbt-d0, *Trem2*$^{-/-}$-mbt-

d0, or *Trem2*$^{+/+}$-mbt-d12. All mice were treated with anti–PD-1 (n = 5 to 7). (**C**) Schematic representation of antibiotic treatment experiment in *Trem2*$^{+/+}$ and *Trem2*$^{-/-}$ during tumor growth. *Trem2*$^{+/+}$ and *Trem2*$^{-/-}$ mice were treated with the indicated antibiotics for 3 weeks before tumor injection and throughout the experiment. (**D**) Tumor growth curve of *Trem2*$^{+/+}$ or *Trem2*$^{-/-}$ treated with either vehicle, ampicillin, or vancomycin. All mice were treated with anti–PD-1 (n = 4 or 5). (B and D) Results are representative of at least two independent experiments and are presented as means ± SEM. (B) Two-way ANOVA followed by post hoc comparisons (Tukey's multiple comparisons test) of time points was used to compare tumor growth across the indicated conditions; statistical significance is indicated for the last time point of the curve. (D) Two-way ANOVA followed by post hoc comparisons (Šidák's multiple comparisons test) of time points was used to compare tumor growth across the indicated conditions; statistical significance is indicated for the last time point of the curve (***P < 0.0001; *P < 0.05; ns = not statistically significant).

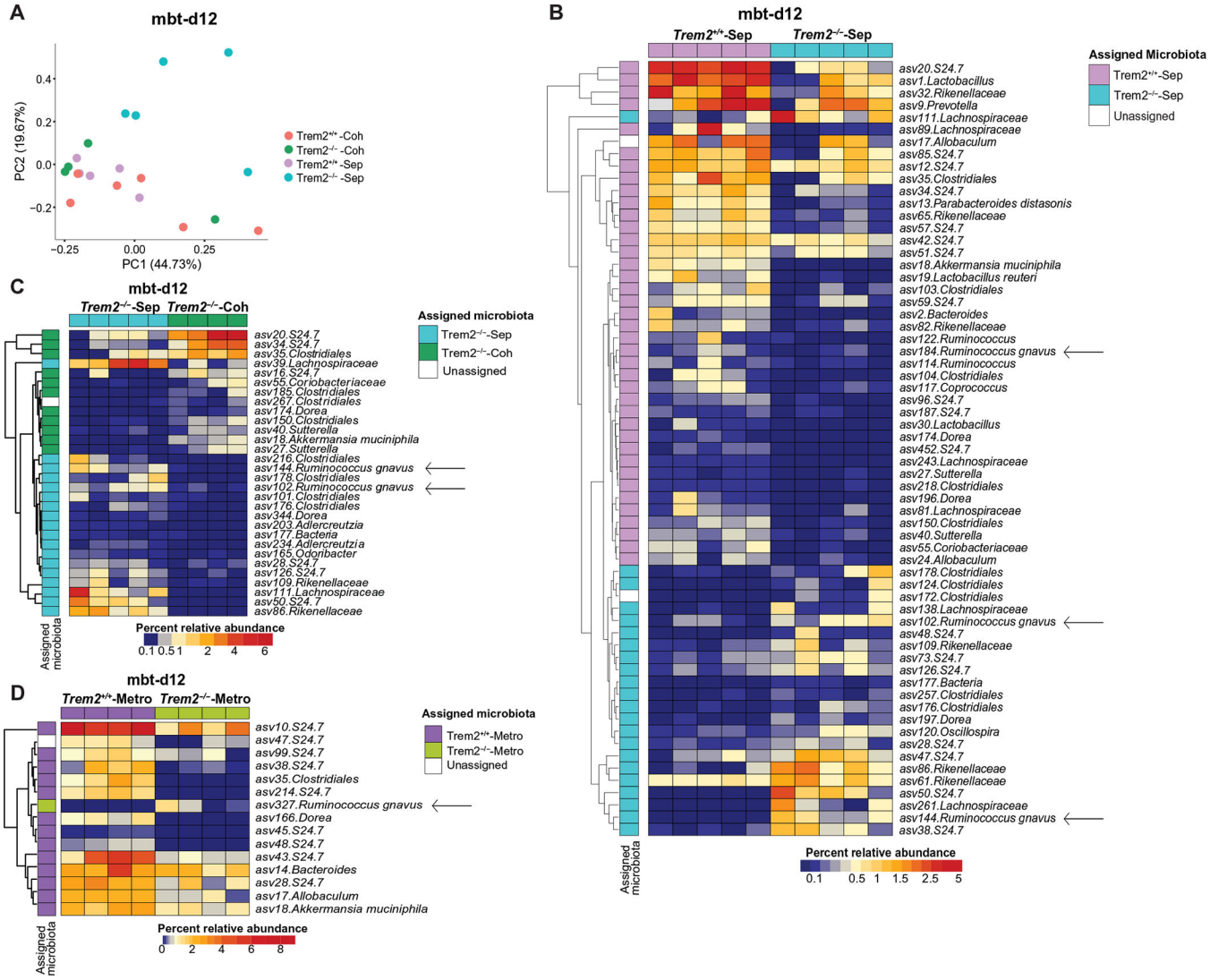

Fig. 3. Increased relative abundance of *R. gnavus* is specifically associated with TREM2 deficiency upon anti–PD-1 treatment.

(**A**) PCoA plots showing beta-diversity analysis performed on the microbiota of *Trem2*$^{+/+}$-Sep, *Trem2*$^{-/-}$-Sep, *Trem2*$^{+/+}$-Coh, and *Trem2*$^{-/-}$-Coh mice. (**B**) Heatmap showing the indicator species analysis performed to compare the fecal microbiota composition of *Trem2*$^{+/+}$-Sep and *Trem2*$^{-/-}$-Sep. (**C**) Heatmap showing the indicator species analysis performed to compare the fecal microbiota composition of *Trem2*$^{-/-}$-Sep and *Trem2*$^{-/-}$-Coh. (**D**) Heatmap showing the indicator species analysis performed to compare the fecal microbiota composition of *Trem2*$^{+/+}$ and *Trem2*$^{-/-}$ mice treated with metronidazole (−Metro). (B to D) Each column represents a different mouse, and each row denotes a different ASV significantly associated with either group. (A to D) All groups were treated with anti–PD-1 and analyzed 3 days after anti–PD-1 injection (mbt-d12).

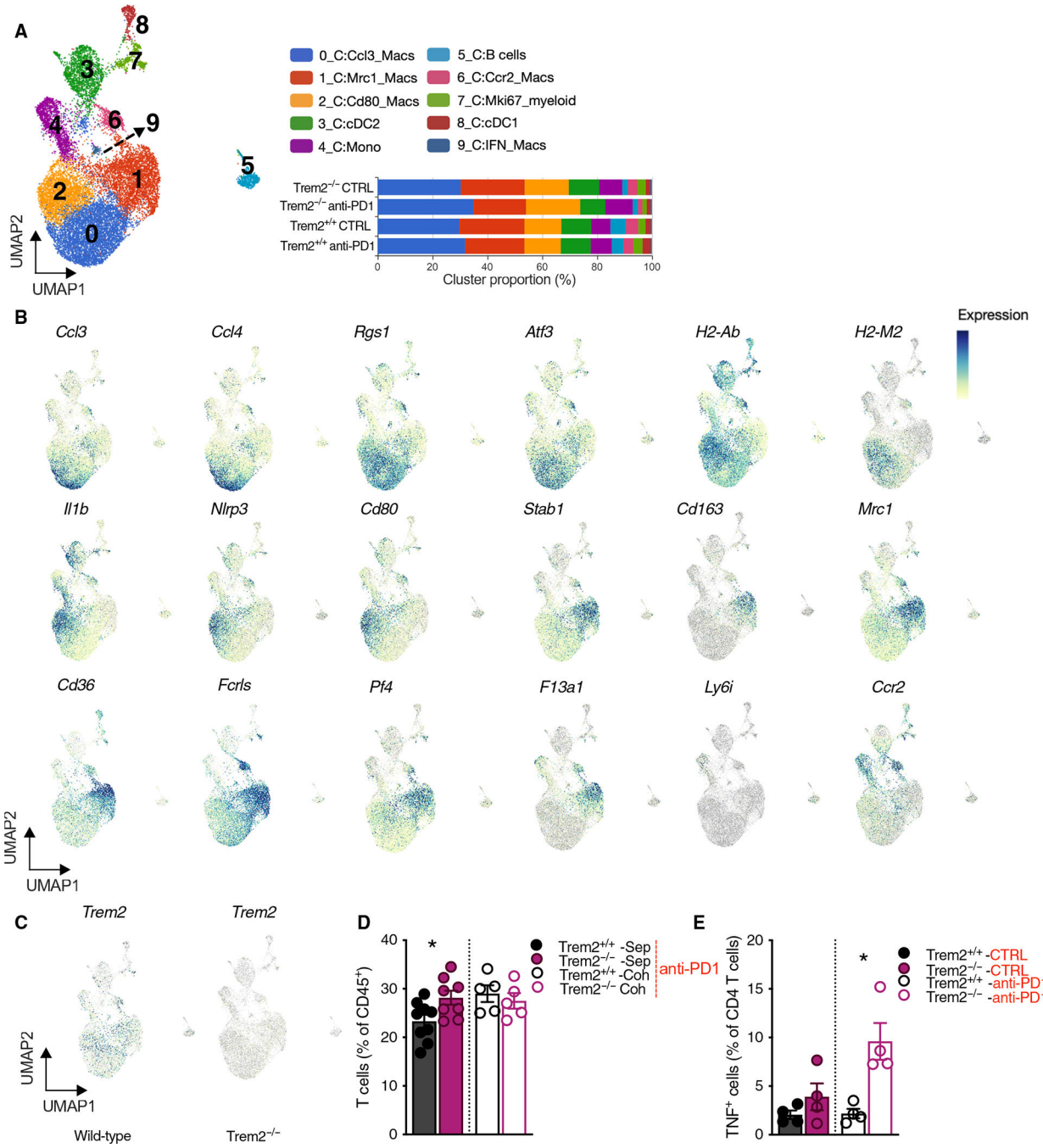

Fig. 4. TREM2 deficiency is associated with a more inflamed colonic environment after anti–PD-1 treatment.

(**A**) UMAP plot showing scRNA-seq of colonic myeloid cell clusters from merged conditions: *Trem2*$^{+/+}$ or *Trem2*$^{-/-}$ treated or not with anti–PD-1 (left). Cells were sorted as live/CD45^{+}Ly6G^{-}SiglecF^{-}/CD11b^{+}. Cluster proportions in each condition: Trem2$^{+/+}$ and *Trem2*$^{-/-}$ treated or not with anti–PD-1 (bottom right panel) (n = 2 mice per group). (**B**) UMAP plots of selected genes from merged conditions. (**C**) UMAP plots showing *Trem2* expression in *Trem2*$^{+/+}$ and *Trem2*$^{-/-}$ mice from merged conditions. (**D**) T cell frequency

in the colon lamina propria in *Trem2*$^{+/+}$ and *Trem2*$^{-/-}$ mice, separated at day 0 (Sep) or co-housed (Coh). All groups were treated with anti–PD-1. (**E**) TNF protein content in *Trem2*$^{+/+}$ and *Trem2*$^{-/-}$ CD4^{+} T cells from mice treated or not with anti–PD-1. (A to E) Samples were analyzed 3 days after anti–PD-1 treatment, 12 days after tumor injection (day 12). (A to C) Each group is representative of two mice that were sequenced separately. (D and E) Results are presented as means ± SEM. Mann-Whitney *U* test was used to compare two groups (**P* < 0.05).

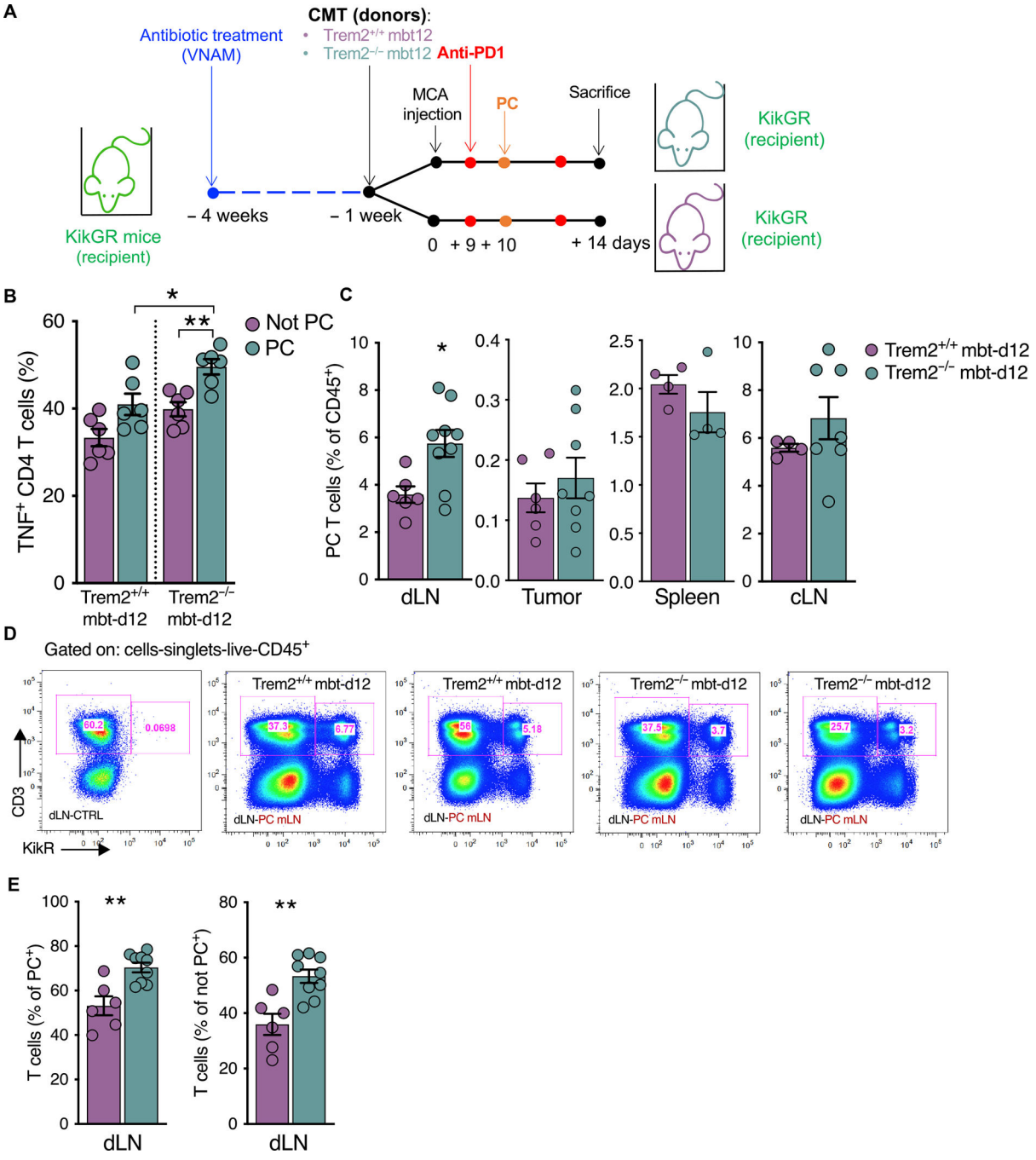

Fig. 5. Microbiota from TREM2-deficient mice promotes T cell activation in the tumor bed.

(**A**) Experimental scheme of CMT in KikGR mice. Mice were treated with a cocktail of antibiotics (VNAM) for 3 weeks before colonization with the cecal content previously collected from either *Trem2*$^{+/+}$ or *Trem2*$^{-/-}$ mice at 3 days after the anti–PD-1 injection (mbt-d12). Mice were treated with anti–PD-1 as indicated and underwent surgery and in situ photoconversion (PC) of mLNs 10 days after tumor injection. Mice were analyzed on day 14 after tumor injection. (**B**) TNF production in PC and not PC CD4^{+} T cells, upon ex vivo restimulation with PMA-ionomycin. Cells were sorted from dLNs. Each dot represents the

pool of two mice. (**C**) Flow cytometry analysis of PC T cells in the indicated organs [dLN, tumor, spleen, and control lymph node (cLN)] in the two groups: KikGR mice transplanted with *Trem2*$^{+/+}$ mbt-d12 or *Trem2*$^{-/-}$ mbt-d12. (**D**) Representative flow plots of PC T cells (KikR^{+}) in dLNs, in the indicated groups. For the control mice (CTRL), mLNs were not photoconverted. (**E**) Flow cytometry analysis of PC and not PC T cells in the dLNs in the indicated groups. (B, C, and E) Results are representative of at least two independent experiments and presented as means ± SEM. Mann-Whitney *U* test was used to compare two groups (* *P* < 0.01; * *P* < 0.05).

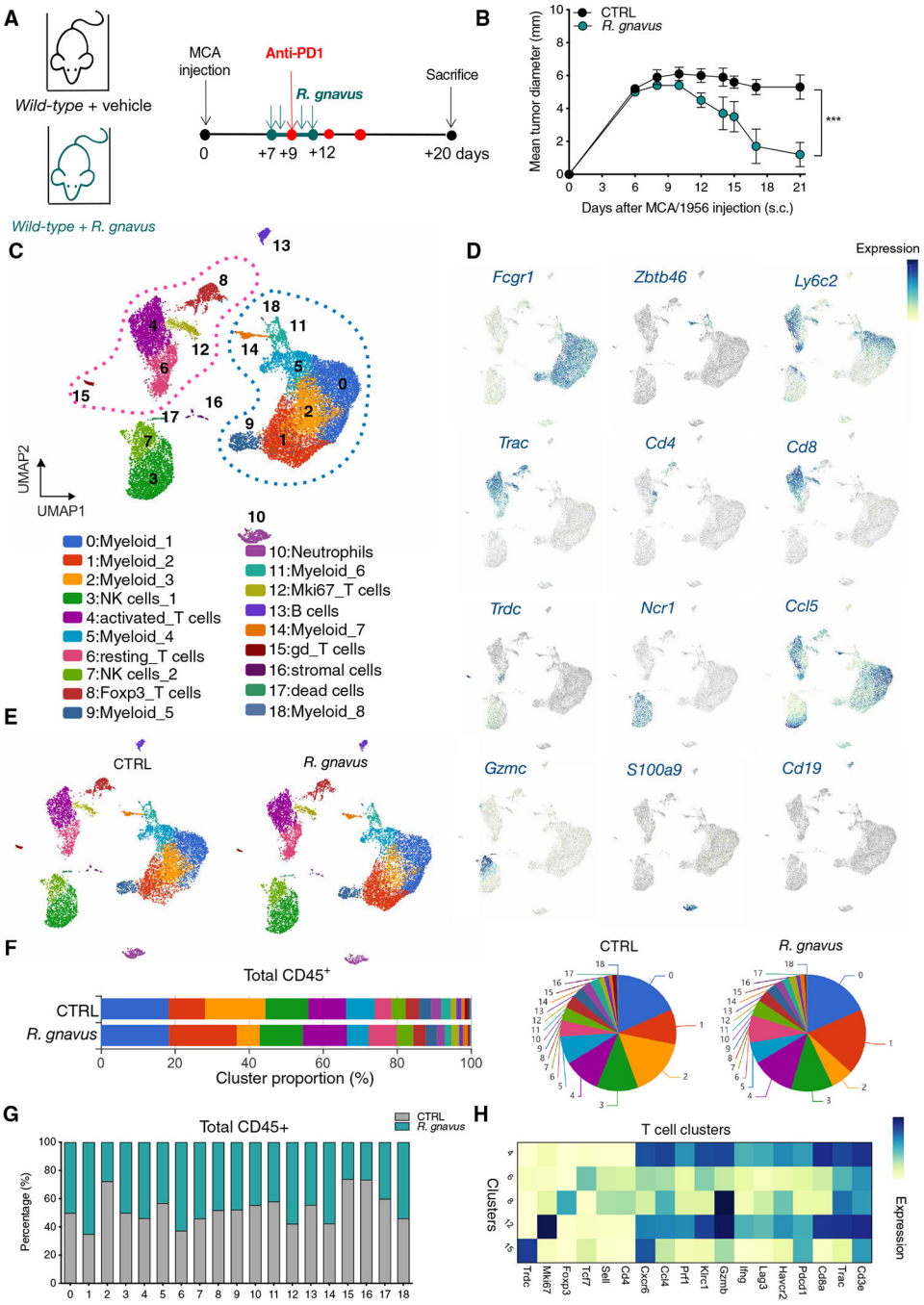

Fig. 6. *R. gnavus* exposure promotes anti–PD-1 response and drives a remodeling of the tumor immune environment.

(**A**) Experimental scheme. Wild-type mice were gavaged with *R. gnavus* (ATCC 29149) or vehicle at the indicated time points. All mice were treated with anti–PD-1. (**B**) MCA/1956 tumor growth in the indicated conditions: wild-type mice treated with vehicle (CTRL) or *R. gnavus*. All mice were treated with anti–PD-1 ($n = 5$). (**C**) UMAP plot showing scRNA-seq of CD45$^+$ cells from tumors from merged conditions obtained. Mice were euthanized on day 14 ($n = 4$ mice per group). (**D**) UMAP plots of selected genes (cluster markers) in CD45$^+$

cell clusters in merged conditions. (**E**) UMAP plots of $CD45^+$ cells in each condition: mice treated with vehicle (CTRL) or *R. gnavus*. (**F**) Cluster proportions of $CD45^+$ cells in the indicated conditions (bar plot and pie charts). (**G**) Bar plot showing the proportion of each group per cluster among the $CD45^+$ cell clusters. (**H**) Heatmap showing the selected genes in the indicated T cell clusters. (A to C) Groups are representative of four mice that were sequenced together and deconvoluted on the basis of a unique hashtag antibody. (B) Results are representative of at least two independent experiments and presented as means ± SEM. Two-way ANOVA followed by post hoc comparisons (Šidák's multiple comparisons test) of time points was used to compare tumor growth across the indicated conditions; statistical significance is indicated for the last time point of the curve ($***P < 0.001$).

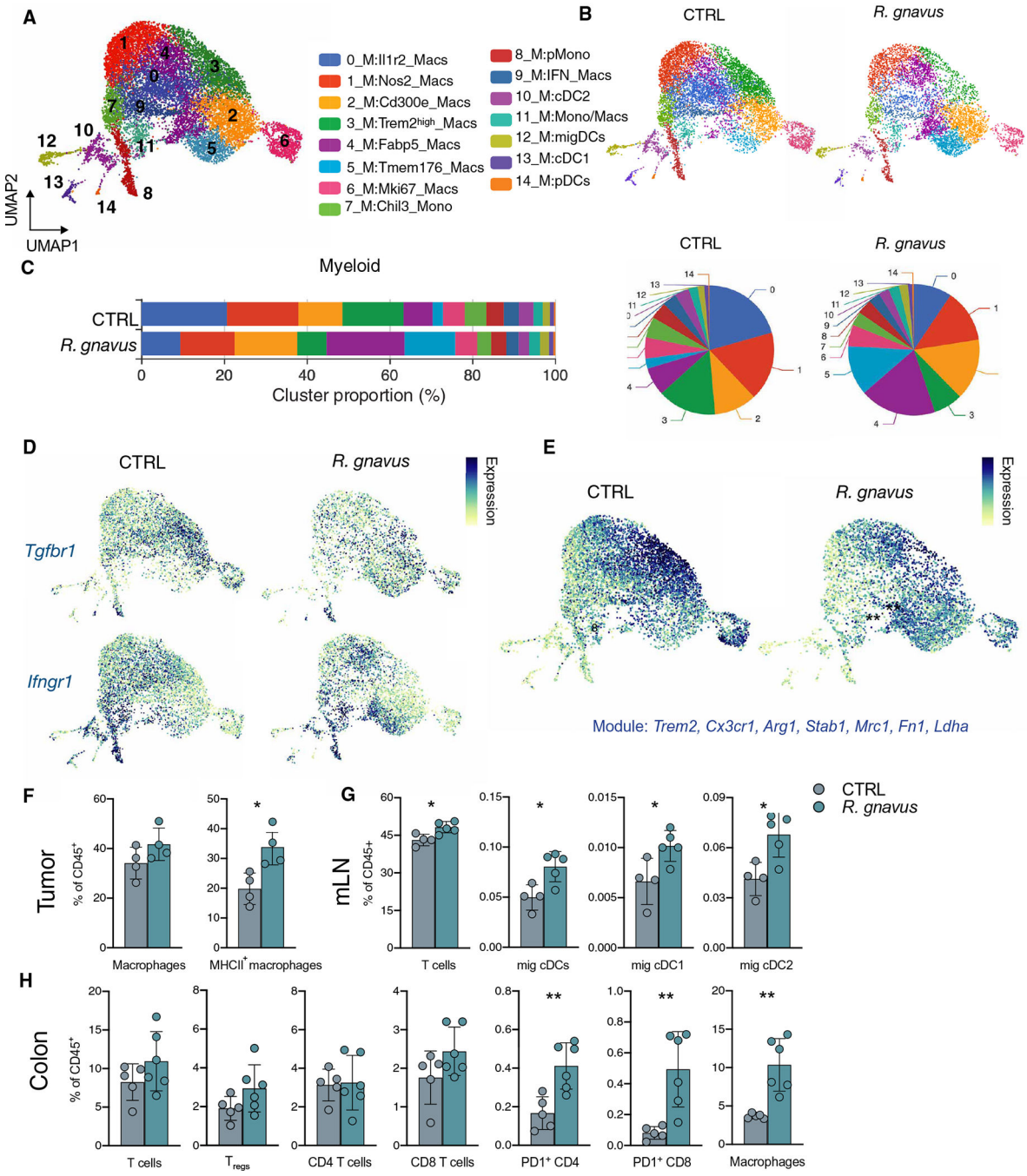

Fig. 7. *R. gnavus* exposure promotes anti–PD-1 response and drives remodeling of the macrophage compartment in the tumor.

(**A**) UMAP plot showing scRNA-seq of myeloid cell clusters after reclustering in merged conditions. (**B**) UMAP plots of myeloid cell clusters in each condition: mice treated with vehicle (CTRL) or *R. gnavus*. (**C**) Cluster proportions of myeloid cell clusters in the indicated conditions (bar plot and pie charts). (**D**) UMAP plots of selected genes (*Tgfbr1* and *Ifngr1*) in myeloid cell clusters in the indicated conditions. (**E**) UMAP plots of manually curated module of the indicated genes associated with immunosuppression in the indicated

conditions. (**F**) Frequency of macrophages in the tumors in the indicated groups. (**G**) Frequency of T cells and migratory dendritic cells (mig cDCs) in mLNs in the indicated groups. (**H**) Frequency of T cells, T cell subsets, and macrophages in colons in the indicated groups. (F to H) Results are presented as means ± SEM. Mann-Whitney *U* test was used to compare two groups (** $P < 0.01$; * $P < 0.05$). (E) One-way ANOVA test was used ($P = 1.2 \times 10^{-41}$). T_{regs}, regulatory T cells.